CTP and *parS* coordinate ParB partition complex dynamics and ParA-ATPase activation for ParABS-mediated DNA partitioning

Running title: CTP- and *parS*-controlled F-plasmid partition

Keywords: Plasmid partition, ParABS system, Chromosome segregation, CTPase

James A. Taylor[1,3], Yeonee Seol[2], Jagat Budhathoki[1], Keir C. Neuman[2] and Kiyoshi Mizuuchi[1*]

[1] Laboratory of Molecular Biology, National Institute of Diabetes and Digestive and Kidney Diseases, National Institutes of Health

[2] Biochemistry and Biophysics Center, National Heart, Lung, and Blood Institute, National Institutes of Health

[3] current address: Alzheimer's Research UK Oxford Drug Discovery Institute, University of Oxford

* Corresponding author: kiyoshimi@niddk.nih.gov

Abstract

ParABS partition systems, comprising the centromere-like DNA sequence *parS,* the *parS*-binding ParB-CTPase and the nucleoid-binding ParA-ATPase, ensure faithful segregation of bacterial chromosomes and low-copy-number plasmids. F-plasmid partition complexes containing $ParB_F$ and $parS_F$ move by generating and following a local concentration gradient of nucleoid-bound $ParA_F$. However, the process through which $ParB_F$ activates $ParA_F$-ATPase has not been defined. We studied CTP- and $parS_F$-modulated $ParA_F$—$ParB_F$ complex assembly, in which DNA-bound $ParA_F$-ATP dimers are activated for ATP hydrolysis by interacting with two $ParB_F$ N-terminal domains. CTP or $parS_F$ enhances the ATPase rate without significantly accelerating $ParA_F$—$ParB_F$ complex assembly. Together, $parS_F$ and CTP accelerate $ParA_F$—$ParB_F$ assembly without further significant increase in ATPase rate. Magnetic-tweezers experiments showed that CTP promotes multiple $ParB_F$ loading onto $parS_F$-containing DNA, generating condensed partition complex-like assemblies. We propose that $ParB_F$ in the partition complex adopts a conformation that enhances $ParB_F$—$ParB_F$ and $ParA_F$—$ParB_F$ interactions promoting efficient partitioning.

Introduction

Faithful segregation of replicated chromosomes is essential for efficient proliferation of cells. Accordingly, many bacteria are equipped with active chromosome and plasmid partition systems belonging to the ParABS family (Baxter and Funnell, 2014; Lutkenhaus, 2012; Vecchiarelli et al., 2012). Basic ParABS systems comprise two proteins, ParA and ParB, and a centromere-like, cis-acting DNA element called *parS*. The ParA proteins of this family are ATPases with a characteristic deviant Walker-A motif (Motallebi-Veshareh et al., 1990) and bind non-specific DNA (nsDNA) in an ATP-dependent manner by forming a DNA binding-competent dimer (Davey and Funnell, 1994; Leonard et al., 2005; Vecchiarelli et al., 2010). Accordingly, ParA proteins localize to the bacterial chromosome (the nucleoid) *in vivo* (Ebersbach and Gerdes, 2004; Hatano et al., 2007; Lim et al., 2014).

ParB is typically a dimeric sequence-specific DNA binding protein that binds tightly to the *parS* consensus sequences that mark the DNA cargo to be partitioned (Bouet et al., 2000; Mori et al., 1989; Pillet et al., 2011; Taylor et al., 2015). Most ParABS systems have multiple copies of a ParB dimer binding consensus sequence that collectively constitute a *parS* site. F-plasmid has a *parS* sequence cluster ($parS_F$, also called *sopC*) composed of twelve repeats of a 16 bp consensus sequence, each separated by 27 base-pair spacer sequences (Helsberg and Eichenlaub, 1986). The ParBs of known chromosomal and plasmid Par systems such as P1 and F bind to *parS via* a helix-turn-helix motif (Schumacher and Funnell, 2005; Schumacher et al., 2010). These HTH-ParB proteins also associate with several kilobases of DNA surrounding a *parS* site *in vivo* in a proximity-dependent manner without obvious sequence specificity (Breier and Grossman, 2007;

49 Murray et al., 2006; Rodionov et al., 1999; Sanchez et al., 2015). This activity, known as ParB
50 spreading, is believed to be essential for proper function of these systems (Breier and Grossman,
51 2007; Graham et al., 2014) and results in the formation of a large nucleo-protein complex (the
52 partition complex) around the *parS* site on the DNA to be partitioned. Mutations in the *B. subtilis*
53 *parB* gene blocking spreading and causing partition deficiency have been identified within the Box
54 II region (GXRR) of the N-terminal domain (Breier and Grossman, 2007; Graham et al., 2014), a
55 highly conserved motif among HTH-ParB homologues (Yamaichi and Niki, 2000). Recently,
56 several groups reported that HTH-ParB proteins have CTPase activity and the Box II residues play
57 key roles in CTP binding and hydrolysis, suggesting that ParB spreading is driven by an active
58 process dependent on energy derived from CTP hydrolysis (Jalal et al., 2020; Osorio-Valeriano et
59 al., 2019; Soh et al., 2019).

60 ParB interacts with ParA *via* its N-terminal region (Ravin et al., 2003) and activates nsDNA-bound
61 ParA dimer's ATPase, releasing it from DNA (Ah-Seng et al., 2009; Davis et al., 1992; Scholefield
62 et al., 2011; Watanabe et al., 1992). In the absence of ParB stimulation, the ATP turnover of ParA
63 is low, typically around one ATP per hour (Ah-Seng et al., 2009; Davis et al., 1992; Fung et al.,
64 2001; Scholefield et al., 2011). Because of this slow basal ATPase rate, and since the majority of
65 cellular ParB molecules is concentrated at the partition complexes due to ParB spreading, ATP
66 hydrolysis by ParA and dissociation from the nucleoid is expected to occur principally in the
67 vicinity of partition complexes. Biochemical studies of P1 ParA ATPase showed a significant
68 time-delay before activation of ParA for DNA binding after ATP binding, predicting a significant
69 free bulk-diffusion period for ParA before reactivation for nsDNA binding (Vecchiarelli et al.,
70 2010). This, along with *in vivo* imaging observations (Hatano et al., 2007; Ringgaard et al., 2009),

71 led to a prediction that the nucleoid proximal to a partition complex would become depleted of
72 ParA (the ParA depletion zone) and the proposal of a diffusion-ratchet model for plasmid
73 segregation by the ParABS system (Vecchiarelli et al., 2010).

74 The diffusion-ratchet model is based on the premise that the nucleoid-bound ParA-ATPase
75 activation by plasmid-bound ParB generates a local ParA depletion zone on the nucleoid, forming
76 a nucleoid-bound ParA concentration gradient around the partition complex (Hu et al., 2017;
77 Vecchiarelli et al., 2010). The interaction of plasmid-bound ParB with the ParA gradient on the
78 nucleoid results in a cargo position-dependent free-energy difference (Sugawara and Kaneko,
79 2011). Binding of ParB to ParA reduces the system free-energy, therefore moving the cargo to a
80 higher ParA concentration lowers the system free-energy. This cargo position-dependent free-
81 energy difference translates to a directional motive force on the ParB bound cargo. The generation
82 of sufficient cargo motive force to overcome thermal diffusion was demonstrated in cell-free
83 reconstitution experiments showing that a bead coated with $parS_F$-containing DNA is driven across
84 an nsDNA-coated flow cell surface in the presence of $ParA_F$, $ParB_F$ and ATP (Vecchiarelli et al.,
85 2014). In some *in vivo* time-lapse imaging experiments ParA has been observed to undergo pole-
86 to-pole oscillations along the length of a nucleoid with a partition complex chasing the receding
87 edge of a ParA distribution zone on the nucleoid, further supporting the diffusion-ratchet model
88 (Hatano et al., 2007; Ringgaard et al., 2009). Variations of this model have also been proposed (Le
89 Gall et al., 2016; Lim et al., 2014; McLeod et al., 2017).

90 Generating persistent directional motion by the diffusion-ratchet model requires a balance between
91 the ParA—ParB association/dissociation dynamics prior to ATP hydrolysis and the steps and

92 kinetic parameters that govern ATP hydrolysis. For example, if every ParA—ParB association
93 resulted in instantaneous ATP hydrolysis and dissolution of the ParA—ParB bonds linking the
94 partition complex (cargo) and the nucleoid, no cargo driving force would result. Conversely, if
95 each bond persisted too long the cargo would remain immobile on the nucleoid (Hu et al., 2017).
96 However, the detailed biochemical reaction steps leading to ParB activation of DNA-bound ParA-
97 ATPase and the subsequent release of ParA have not been determined.

98 In order to advance our quantitative understanding of the ParABS system mechanism, we
99 investigated the assembly and disassembly kinetics of $ParA_F$—$ParB_F$ complexes that form prior to
100 ATP hydrolysis using F-plasmid $ParA_FB_FS_F$ (also called SopA/B/C) as a model system. Employing
101 a TIRF microscopy-based nsDNA-carpet assay (Vecchiarelli et al., 2013) we first examined the
102 stoichiometry of the nsDNA-bound $ParA_F$—$ParB_F$ complexes that accumulate in the absence of
103 ATP hydrolysis. We investigated impacts of different $ParB_F$-cofactors (*$parS_F$* and CTP) or $ParB_F$
104 mutations that hinder $ParB_F$ dimerization, *$parS_F$*-binding, CTPase activity, or $ParA_F$ ATPase
105 activation. We then studied how the same set of cofactors or $ParB_F$ mutations influenced $ParA_F$-
106 ATPase activation by $ParB_F$. Our results showed that $ParB_F$ formed complexes with nsDNA-bound
107 $ParA_F$ in which both $ParB_F$-interacting faces of the $ParA_F$ dimers were occupied by the N-terminal
108 $ParA_F$-activation domain of $ParB_F$. All such complexes observed in the presence of ATPγS
109 exhibited similar, slow dissociation kinetics from nsDNA compared to $ParA_F$ dimers in the absence
110 of $ParB_F$ so long as both $ParB_F$-interacting faces of the $ParA_F$ dimers were occupied by $ParB_F$ N-
111 terminal domains. Binding of $ParB_F$ N-terminal domains at both $ParB_F$-interaction faces is also
112 necessary for efficient ATPase activation of nsDNA-bound $ParA_F$ dimers. Strikingly, the $ParB_F$
113 cofactors, CTP and *$parS_F$*, acted synergistically to accelerate the assembly of pre-ATP hydrolysis

114 $ParB_F$—$ParA_F$ complexes on nsDNA. In addition, a magnetic tweezers-based DNA condensation
115 assay revealed that stable DNA condensation by $ParB_F$ required both CTP and $parS_F$. These
116 observations suggested that CTP and $parS_F$ promote both $ParA_F$—$ParB_F$ and $ParB_F$—$ParB_F$
117 interactions. The compaction of $parS_F$-containing DNA by $ParB_F$ in the presence of CTP
118 recapitulated the salient features of the condensed ParB spreading partition complex observed *in*
119 *vivo*, suggesting that $ParB_F$ in the presence of $parS_F$ and CTP closely reflects the functional state
120 of $ParB_F$ in the partition complexes *in vivo*. Interestingly, $ParB_F$ in these conditions accelerated
121 ATP turnover by the nsDNA-bound $ParA_F$ no more than two-fold compared to $ParB_F$ without $parS_F$
122 and CTP, to a modest ~80 h^{-1}. These findings have important implications for the diffusion-ratchet
123 model of F-plasmid partition by the ParAB*S* system.

124
125 **Results**

126 Here, we investigated the ParA—ParB interactions that lead to accelerated ATP hydrolysis by
127 ParA and how they are impacted by $parS_F$ and CTP. First, we addressed the nature of nsDNA-
128 bound $ParA_F$—$ParB_F$ complexes. In the presence of ATP, $ParA_F$ forms DNA binding-competent
129 dimers and binds the nsDNA-carpet without $ParB_F$. Upon forming a complex with $ParB_F$, $ParA_F$
130 becomes activated for ATP hydrolysis and the complex rapidly disassembles (Vecchiarelli et al.,
131 2013), impeding characterization of the complex. Therefore, we studied DNA-bound $ParA_F$—
132 $ParB_F$ complexes that accumulate prior to ATP hydrolysis by using non-hydrolysable ATPγS.
133 $ParA_F$ is not expected to form DNA binding competent dimers efficiently in the presence of ATPγS
134 based on the study of the closely related $ParA_{P1}$ ATPase (Vecchiarelli et al., 2010). However, we
135 found $ParB_F$ promotes conversion of $ParA_F$ to a DNA binding competent state in the presence of

136 ATPγS (see below). Hence in this study, we infused $ParA_F$-eGFP and $ParB_F$-Alexa647, or other
137 fluorescent-labeled $ParB_F$ variants, preincubated at room temperature for 10 min with ATPγS into
138 an nsDNA-carpeted flow cell and quantified the densities of the two DNA-associated proteins by
139 imaging the flow cell surface with TIRF microscopy (Figure 1). $ParA_F$ alone at the concentration
140 used here (1 μM, all protein concentrations are expressed as monomer concentrations) does not
141 efficiently bind DNA in the presence of ATPγS as expected, and only low-level steady state
142 density (less than ~ 200 monomers per μm^2) of $ParA_F$-eGFP was detected on the DNA-carpet
143 (Figure 2A, B). The observed DNA dissociation rate constant of $ParA_F$-ATPγS (~6 min^{-1}) is similar
144 to that of $ParA_F$-ATP estimated by FRAP, or by washing the flow-cell with nsDNA-containing
145 buffer (~4.5 – 6 min^{-1}, Vecchiarelli, 2013). $ParB_F$-Alexa647 (2 μM) did not bind the DNA-carpet
146 to a significant level in the 300 mM K-glutamate buffer used in this experiment.

147 *The N-terminus of $ParB_F$ alone enhances DNA binding activity of $ParA_F$.*

148 We first examined if the N-terminal $ParA_F$-activation domain of $ParB_F$ ($ParB_F^{1-42}$) alone can induce
149 the $ParA_F$ conformational changes necessary for DNA binding in the presence of ATPγS. The
150 activation domain includes Arginine 36, which is critical for activation of $ParA_F$ ATPase (Ah-Seng
151 et al., 2009; Leonard et al., 2005), but lacks the CTPase- (AA63-155), *$parS_F$*-binding- (AA160-
152 272), and dimerization- (AA276-323) domains. For these experiments we used $ParB_F^{1-42}$ fused to
153 the N-terminus of mCherry ($ParB_F^{1-42}$-mCherry). This protein is a monomer in solution as judged
154 by its elution profile on a gel filtration column (Figure 2—figure supplement 1). $ParB_F^{1-42}$-mCherry
155 (10 μM) and $ParA_F$-eGFP (1 μM) bound the DNA-carpet together in the presence of ATPγS to a
156 density of ~5000 monomers/μm^2 maintaining ~1:1 stoichiometry (Figure 2C). When washed with

157 a buffer containing ATPγS, $ParB_F^{1-42}$-mCherry dissociated first, with an apparent dissociation rate
158 constant of ~5.7 min^{-1}, closely followed (within a few seconds) by $ParA_F$-eGFP dissociation
159 (Figure 2D). On the other hand, when the wash buffer contained 10 μM $ParB_F^{1-42}$-mCherry and
160 ATPγS, both proteins dissociated together, significantly slower than $ParA_F$-eGFP bound to the
161 DNA-carpet alone, with an apparent rate constant of ~0.9 min^{-1}, maintaining ~1:1 stoichiometry
162 (Figure 2E). After essentially complete dissociation of $ParA_F$-eGFP from the DNA-carpet, 10 μM
163 $ParB_F^{1-42}$-mCherry present in the wash solution showed no significant binding to the DNA-carpet,
164 indicating low intrinsic affinity of this protein for DNA. FRAP measurements of $ParA_F$-eGFP—
165 $ParB_F^{1-42}$-mCherry bound in steady state to the DNA-carpet in the presence of ATPγS also
166 indicated rapid exchange of $ParB_F^{1-42}$-mCherry (Figure 2—figure supplement 2). Thus, at
167 saturating $ParB_F^{1-42}$-mCherry concentration, a $ParA_F$—ATPγS dimer is bound by two molecules of
168 $ParB_F^{1-42}$-mCherry occupying both sides of the $ParA_F$ dimer. The data also indicate that $ParA_F$
169 dimers adopt a state of slowed dissociation from nsDNA when both of the $ParB_F$-interacting faces
170 are occupied by the $ParB_F$ N-terminal domain. The nsDNA dissociation rate constants of $ParA_F$—
171 $ParB_F$ complexes (including those involving $ParB_F$ variants) and $ParB_F$:$ParA_F$ stoichiometry
172 reported above and in the following sections are summarized in Table 1.

173 *$ParA_F$ ATPase activation requires binding of two copies of $ParB_F$ N-terminal domain to the $ParA_F$*
174 *dimer.*

175 $ParB_F^{1-42}$ stimulated $ParA_F$-ATPase (1 μM) with a clear sigmoidal $ParB_F^{1-42}$ concentration
176 dependence and a half-maximum activation concentration of ~1.2 μM (Figure 2F; Table 2). Thus,
177 monomeric $ParB_F^{1-42}$ appears to activate $ParA_F$-ATPase when it binds on both sides of the DNA-

178 bound $ParA_F$ dimers. To test if the observed sigmoidal concentration dependence is due to the
179 monomeric nature of $ParB_F^{1-42}$, we prepared the N-terminal region of $ParB_F$ fused to mCherry and
180 the nuclease activity deficient $EcoRI^{E111Q}$, $ParB_F^{1-42}$-mCherry-$EcoRI^{E111Q}$ (see Figure—2 figure
181 supplement 3A). This construct, with expected EcoRI dimerization K_D < 20 pM (Modrich and
182 Zabel, 1976), efficiently activated $ParA_F$-ATPase at least to a similar maximum rate as $ParB_F^{1-42}$,
183 but with a K_{half} of ~0.15 μM, ~8-fold lower than $ParB_F^{1-42}$, and displayed no noticeable sigmoidal
184 concentration dependence (Figure 2G). Potential binding of the inactive EcoRI domain to DNA
185 did not appear to influence the ATPase activation properties of this construct; addition of EcoRI-
186 binding DNA fragment in the reaction did not impact the ATPase activation (Figure 2—figure
187 supplement 4). Based on these results, we conclude that both $ParB_F$-binding faces of a $ParA_F$ dimer
188 must be occupied by $ParB_F$ N-termini for stimulation of its ATPase activity.

189 *$ParB_F^{1-42\ R36A}$ forms a rapidly disassembling complex with $ParA_F$ on the DNA carpet.*

190 An R36A mutation was reported to significantly compromise $ParB_F$'s ability to activate $ParA_F$'s
191 ATPase (Ah-Seng et al., 2009). To test whether this mutation affected $ParB_F$'s ability to form a
192 complex with $ParA_F$ we repeated the experiments shown in Figure 2C-E using $ParB_F^{1-42\ R36A}$-
193 mCherry. $ParB_F^{1-42R36A}$-mCherry and $ParA_F$-eGFP bound with an approximately 1:1 stoichiometry,
194 similar to $ParB_F^{1-42}$-mCherry but reached a steady-state density on the DNA-carpet of less than
195 10% of the density observed with $ParB_F^{1-42}$-mCherry (Figure 3A). When washed with buffer
196 containing ATPγS, $ParB_F^{1-42\ R36A}$-mCherry disassociated first followed by $ParA_F$, similar to the
197 results obtained with $ParB_F^{1-42}$-mCherry but $ParB_F^{1-42\ R36A}$-mCherry dissociated ~10-fold faster,
198 followed by dissociation of $ParA_F$-eGFP within a few seconds (Figure 3B). When the wash buffer

199 also contained 10 μM $ParB_F^{1-42\ R36A}$-mCherry the two proteins dissociated in parallel maintaining
200 ~1:1 stoichiometry (Figure 3C). Together these observations indicate that $ParB_F^{R36A}$ interacts with
201 $ParA_F$, but with a much faster dissociation rate constant compared to wild-type $ParB_F$. $ParB_F^{1-42\ R36A}$
202 could activate $ParA_F$-ATPase with an increased half-saturation concentration of 108 μM,
203 approximately 100-fold higher than $ParB_F^{1-42}$ (Figure 3D). These results explain the puzzling report
204 that while the R36A mutation severely compromised activation of $ParA_F$-ATPase by $ParB_F$, it did
205 not impede oscillation of $ParA_F$ on the nucleoid, and only mildly reduced plasmid stability (Ah-
206 Seng et al., 2013). At the interface between the $ParA_F$-bound nucleoid and partition complexes
207 containing many $ParB_F$ dimers, the local $ParB_F$ concentration is expected to be sufficiently high
208 for this mutant protein to activate $ParA_F$-ATPase to effectively generate a $ParA_F$ depletion zone
209 and motive force driving the partition complex as indicated by the repeated oscillation of the
210 nucleoid-bound $ParA_F$ distribution.

211 *$ParA_F$ and $ParB_F$ bind to and dissociate from nsDNA together in the presence of ATPγS with ~1:1*
212 *stoichiometry.*

213 When $ParA_F$-eGFP and full-length $ParB_F$-Alexa647 were incubated together at 1 μM and 2 μM,
214 respectively in the presence of ATPγS, they bound to the DNA-carpet in parallel maintaining ~1:1
215 stoichiometry up to a density of ~5000 monomers/μm^2 (Figure 4A). They also dissociated from
216 the DNA-carpet in parallel, maintaining ~1:1 stoichiometry, when washed with a buffer containing
217 ATPγS, with an apparent dissociation rate constant of approximately ~1 min^{-1} (Figure 4B). These
218 results show that $ParA_F$ and $ParB_F$ form a hetero-tetramer containing two monomers each of $ParA_F$

219 and $ParB_F$ (A_2B_2), or larger oligomers composed of the hetero-tetramers, that binds as a unit on
220 nsDNA in the presence of ATPγS.

221 Full-length $ParB_F$, which forms dimer with apparent K_D of ~ 19 nM (Figure 4—figure supplement
222 1), activated $ParA_F$-ATPase in the presence of nsDNA to ~50 hr^{-1} without significant sigmoidal
223 concentration dependence (Figure 4E). Based on the results of experiments with monomeric
224 $ParB_F^{1-42}$ proteins described earlier, we conclude that a single dimer of full-length $ParB_F$ can
225 straddle an nsDNA-bound $ParA_F$ dimer, permitting the two N-termini to interact with both of the
226 $ParB_F$-binding faces of the $ParA_F$ dimer to activate the ATPase.

227 *In the presence of $parS_F$, $ParB_F$ forms a 2:1 complex with $ParA_F$.*

228 We next asked if $ParB_F$ bound to $parS_F$ interacts differently with $ParA_F$ on the DNA-carpet. We
229 preincubated $ParA_F$-eGFP, $ParB_F$-Alexa647, ATPγS and a 24 bp duplex DNA fragment containing
230 a single $parS_F$ consensus sequence, at a slight molar excess over $ParB_F$ dimer, for 10 min at room
231 temperature. At the concentrations used, most of the $ParB_F$ dimers are expected to be bound to
232 $parS_F$. When infused into the DNA-carpeted flow cell, $ParA_F$-eGFP and $ParB_F$-Alexa647 bound to
233 and dissociated from the carpet with a stoichiometry of ~1:2 (Figure 4C, D), in sharp contrast to
234 the ~1:1 stoichiometry without $parS_F$ DNA. The kinetic parameters of the complex assembly and
235 disassembly were not significantly affected. These results demonstrate that $ParA_F$ and $ParB_F$ form
236 a complex of one $ParA_F$ dimer and two $ParB_F$ dimers (A_2B_4) in the presence of $parS_F$.

237 Does the change in protein stoichiometry caused by $parS_F$ translate to different levels of $ParA_F$-
238 ATPase activation? A previous study, comparing plasmid DNA with and without $parS_F$ as the

239 cofactor, showed that $ParB_F$ activates $ParA_F$-ATPase a few-fold more efficiently in the presence
240 of plasmid DNA containing a full $parS_F$ site (Ah-Seng et al., 2009). We titrated $ParB_F$ in the
241 presence of $ParA_F$, pBR322 DNA and 24 bp $parS_F$ duplex at a stoichiometric excess concentration
242 over the $ParB_F$ dimer. In the presence of $parS_F$ DNA, $ParB_F$ activated $ParA_F$-ATPase to a maximum
243 turnover rate of ~80 hr^{-1}, a ~60% increase compared to reactions where the $parS_F$ fragment was
244 replaced with a scrambled sequence fragment (Figure 4E). These results indicate that a single $parS_F$
245 DNA-bound $ParB_F$ dimer cannot straddle an nsDNA-bound $ParA_F$ dimer to activate the ATPase,
246 but by binding two $ParB_F$ dimers the ATPase activation level reaches slightly higher level than in
247 the absence of $parS_F$ DNA.

248 We note that $ParB_F^{R121A}$, harboring a mutation in the conserved Box II region of the CTPase domain,
249 neither exhibited a change in the $ParB_F$/$ParA_F$ complex stoichiometry, nor a change in the $ParB_F$-
250 stimulated ATP turnover, in response to $parS_F$ (Figure 4—figure supplement 2), suggesting that
251 the effects of $parS_F$ binding described above are mediated through conformational changes in the
252 CTPase domain (see below for further discussion).

253 *CTP alters the complex formed between $ParA_F$ and $ParB_F$ in a manner similar to $parS_F$, and*
254 *accelerates complex formation in the presence of $parS_F$.*

255 ParB proteins have recently been reported to have CTPase activity that is coupled to changes in
256 their DNA binding properties and refolding of the CTPase domains into a globular dimeric
257 structure in the presence of CTP (Soh et al., 2019; Osorio-Valeriano et al., 2019) from the more
258 extended and poly-dispersed structure in the absence of nucleotide (Chen et al., 2015). We
259 therefore decided to test if the addition of CTP influences the $ParA_F$—$ParB_F$ complex formed on

260 the DNA-carpet in the presence of ATPγS. When $ParA_F$-eGFP and $ParB_F$-Alexa647 were
261 incubated together in the presence of ATPγS (1 mM) and CTP (2 mM), they bound to and
262 dissociated from the nsDNA-carpet with a stoichiometry of ~1:2 (Figure 5A, Figure 5—figure
263 supplement 1A). The assembly kinetics of the carpet-bound complex was roughly the same as in
264 the absence of CTP, however the apparent dissociation rate constant during buffer wash was
265 slightly but reproducibly slower by a factor of roughly two at ~ 0.6 min^{-1}. When $parS_F$ was included
266 together with CTP, the rate of A_2B_4 complex assembly on the DNA-carpet increased several-fold,
267 the binding density of the complex on the DNA-carpet reached a correspondingly higher level, and
268 the two proteins dissociated from the DNA-carpet maintaining a ~1:2 stoichiometry with apparent
269 dissociation rate constant similar to that in the absence of $parS_F$ (Figure 5B, Figure 5—figure
270 supplement 1B). When CTP was replaced by CDP in the presence of $parS_F$, although the
271 $ParB_F$/$ParA_F$ ratio remained above 2, unlike in the presence of CTP the complex assembly rate did
272 not increase (Figure 5C, Figure 5—figure supplement 1C), thus behaving similarly to the reaction
273 in the presence of $parS_F$ alone.

274 Next, we asked if the $parS_F$ DNA fragment was incorporated in the A_2B_4 complexes assembled in
275 its presence. The experiments in the presence of $parS_F$ were repeated in the presence or absence of
276 CTP with $ParA_F$ (1 μM), $ParB_F$-Alexa647 (2 μM) and Alexa488-$parS_F$ (1.1 μM), and the nsDNA-
277 carpet-bound ratio of $parS_F$ and $ParB_F$ after 240 sec sample infusion was measured (Figure 5D).
278 The observed $parS_F$ / $(ParB_F)_2$ ratio in the absence of CTP was ~0.2, while in the presence of CTP,
279 the ratio was only ~0.04. Thus, whereas the assembly of the A_2B_4 complex involving CTP-$ParB_F$
280 was accelerated by $parS_F$, a very small fraction of the resulting complex contained the $parS_F$-DNA
281 fragment, indicating that $parS_F$ plays a catalytic role in the activation of CTP-$ParB_F$ and accelerated

282 assembly of the A_2B_4 complex. This parallels the observation that a much lower concentration of
283 *parS*$_F$ fully activated the CTPase activity of $ParB_F$ (Figure 5—figure supplement 2C) as has also
284 been shown for $ParB_{Bsu}$ (Soh et al., 2019).

285 *ParB*$_F$ *activates ParA*$_F$*-ATPase to the full extent without parS*$_F$ *in the presence of CTP*.

286 The maximum $ParB_F$ activation of $ParA_F$-ATPase in the presence of CTP, with or without *parS*$_F$,
287 was comparable to that of *parS*$_F$-bound $ParB_F$ in the absence of CTP (Figure 5E, F). The half-
288 saturation concentration of $ParB_F$ in the presence of *parS*$_F$ and CTP was significantly lower than
289 in the absence of CTP (~0.24 μM *vs* ~0.6 μM). Combined with the observation of faster assembly
290 of the complex on the DNA-carpet, a likely possibility is that in the presence of CTP and *parS*$_F$,
291 the $ParB_F$ dimer adopts a unique state that interacts with $ParA_F$ dimers with a higher association
292 rate constant. We note that the $ParA_F$-ATPase assays in this study measured radioactive γ-
293 phosphate release from γ-^{32}P-ATP, avoiding potential technical complications associated with
294 ATPase measurements in the presence of CTP.

295 We next measured the $ParB_F$-CTPase activity to estimate the apparent K_M and k_{cat} of $ParB_F$ for CTP
296 hydrolysis in the presence and absence of *parS*$_F$. $ParB_F$ had negligible activity for all NTPs other
297 than CTP (Figure 5—figure supplement 2A), and the CTP hydrolysis rate increased with a
298 hyperbolic CTP concentration dependence, which could be fit with the Michaelis-Menten equation
299 with apparent K_M of ~8 μM and ~18 μM and maximum turnover rates of ~14 h^{-1} and ~44 h^{-1} in the
300 absence and presence of *parS*$_F$ DNA, respectively (Figure 5—figure supplement 2B). Thus, 2 mM
301 CTP used in the experiments of Figure 5 should have remained saturating $ParB_F$ for the duration

302 of the reaction. Stimulation of the CTPase activity by *parS*$_F$ exhibited a pronounced sigmoidal
303 concentration dependence approaching saturation at ~ 60 nM, well below the ParB$_F$ concentration
304 in the reaction (0.84 μM) (Figure 5—figure supplement 2C).

305 During these experiments, which were prompted by a reviewer's comment, we also attempted to
306 characterize the interaction between CDP and ParB$_F$, but discovered that the CDP used here
307 contained ~2% contamination of a compound that released Pi upon incubation with ParB$_F$ (Figure
308 5—figure supplement 2D). The results shown in Figure 5C and Figure 5F suggest this
309 contamination did not strongly influence the reactions involving CDP, considering that they
310 generally paralleled the results obtained in the absence of C-nucleotides with only minor deviations.
311 However, this contamination prevented us from accurately determining the affinity of ParB$_F$ for
312 CDP.

313

314

315

316

317

318

319

320

321 Table 1. *Apparent disassembly or exchange rate constants (min^{-1}) and ParB$_F$/ParA$_F$ ratio*
322 *from fits of TIRFM wash and FRAP experiments.*

Protein Measured		$ParA_F$	$ParA_F$ + $ParB_F^{1-42}$		$ParA_F$ + $ParB_F^{1-42\ R36A}$		FRAP		$ParA_F$ + $ParB_F$		$ParA_F$ + $ParB_F$ + CDP		$ParA_F$ + $ParB_F$ + CTP		$ParA_F$ + $ParB_F^{R121A}$	
		$ParA_F$ -eGFP	*$ParA_F$ -eGFP*	*$ParB_F$ -Alexa647*	*$ParA_F$ -eGFP*	*$ParB_F^{1-42\ R36A}$ -mCherry*	*$ParA_F$ -eGFP*	*$ParB_F^{1-42}$ -mCherry*	*$ParA_F$ -eGFP*	*$ParB_F$ -Alexa647*	*$ParA_F$ -eGFP*	*$ParB_F$ -Alexa647*	*$ParA_F$ -eGFP*	*$ParB_F$ -Alexa647*	*$ParA_F$ -eGFP*	*$ParB_F^{R121A}$ -Alexa647*
- *$parS_F$*	k_{off}	**6.4± 0.6 N=4 (12)**	**5.2± 0.2 N=2 (9)**	**6.3± 0.3 N=2 (9)**	**29± 2 N=3 (9)**	**52± 4 N=3 (9)**	**2.00± 0.08 N=3 (11)**	**15± 2** N=3 (12)**	**0.93± 0.07 N=2 (6)**	**0.89± 0.09 N=2 (6)**	*N.D.*	*N.D.*	**0.63± 0.04 N=2 (7)**	**0.65± 0.1 N=2(7)**	**0.89± 0.01 N=3 (8)**	**0.78± 0.05 N=3 (8)**
	A:B		*1 : 1.27± 0.06 N=2 (8)*		*1 : 0.92± 0.02*** N=3 (9)*				*1 : 1.1± 0.1 N=3 (9)*				*1 : 2.2± 0.2 N=3 (10)*		*1 : 0.99± 0.01 N=3 (8)*	
+ *$parS_F$*	k_{off}	*N.D.*	*N.D.*		*N.D.*		*N.D.*		**0.95± *0.04* N=2 (6)**	**0.82± *0.01* N=2 (6)**	**0.46± 0.02 N=2 (7)**	**0.53± 0.01 N=2 (7)**	**0.60± 0.08 N=2 (5)**	**0.83± 0.12 N=2 (6)**	**0.91± 0.01 N=3 (8)**	**0.78± 0.04 N=3 (8)**
	A:B								*1 : 2.2± 0.4 N=3 (9)*		*1 : 2.53± 0.07 N=2 (6)*		*1 : 2.2± 0.3 N=2(6)*		*1 : 1.12± 0.01 N=3 (12)*	
$ParB_F^{1-42}$ or $ParB_F^{1-42\ R36A}$ in wash	k_{off}	*N.D.*	**0.84± 0.01* N=1 (3)**	**0.89± 0.02* N=1 (3)**	**1.8± 0.4 N=3 (9)**	**1.8± 0.4 N=3 (9)**	*N.D.*		*N.D.*		*N.D.*		*N.D.*		*N.D.*	

Table 2: ATPase fit parameters.

	$ParB_F$		$ParB_F$ CTP		$ParB_F$ CDP	$ParB_F^{R121A}$		$ParB_F^{1-42}$	$ParB_F^{1-42}$ R36A	$ParB_F^{1-42}$-mCherry-$EcoRI^{E111Q}$	
	Scram	*$parS_F$*	*Scram*	*$parS_F$*	*$parS_F$*	*Scram*	*$parS_F$*	N = 6	N = 3	*Scram*	*EcoRI DNA*
	N = 6	N = 6	N = 3	N = 3	N = 3	N = 3	N = 3			N = 3	N = 2
v_{max} (hr^{-1})	54 *± 5*	79 *± 2*	79 *± 8*	78 *± 8*	87 *± 5*	60 *± 5*	62 *± 5*	83 *± 3*	38 *± 2*	131 *± 13*	125 *± 9*
K_A (µM)	0.53 *± 0.09*	0.59 *±0.03*	0.41 *± 0.05*	0.24 *±0.02*	0.34 *±0.04*	0.86 *± 0.1*	1.1 *± 0.1*	1.2 *± 0.1*	108 *± 13*	0.16 *± 0.04*	0.16 *± 0.03*
Cooperativity coefficient (n)	1.2 *± 0.2*	1.4 *± 0.1*	3.3 *± 1.0*	3.6 *± 0.2*	1.1 *± 0.1*	2.5 *± 0.6*	1.6 *± 0.3*	2.5 *± 0.3*	1.5 *± 0.2*	1.4 *± 0.3*	1.4 *± 0.2*

In the presence of CTP, $ParB_F$ condenses DNA carrying $parS_F$ in cis.

331 The recently discovered CTP and *parS* dependent ParB conformational change appears to promote
332 ParB *parS*-DNA binding and spreading (Soh et al., 2019), impacting ParB-DNA partition complex
333 assembly. *In vivo*, spreading ParB forms condensed foci around *parS* sites indicating that *parS*
334 driven ParB spreading likely occurs *in cis*. Nonetheless, the possibility that *parS* can trigger ParB
335 spreading *in trans* has not been tested *in vitro*. Previous studies reported DNA condensation by *B.*
336 *subtilis* ParB *via* ParB—ParB interactions, but these studies were conducted in the absence of CTP
337 and did not observe a strong effect of *parS in cis* (Graham et al., 2014; Song et al., 2017; Taylor
338 et al., 2015). To see if $parS_F$ can act *in-trans* and to characterize how $parS_F$ and CTP influence
339 $ParB_F$—DNA interactions *in vitro*, we conducted single-molecule DNA pulling experiments
340 employing magnetic tweezers. $ParB_F$ at various concentrations was infused into a flow cell
341 containing ~ 5 kbp DNA tethers that anchored magnetic beads to the coverslip surface (Figure 6A).
342 The tethers contained either twelve $parS_F$ consensus sequence repeats at their midpoints ($parS_F$-
343 DNA), or no $parS_F$ sequence (nsDNA). The protein sample was infused while the DNA tethers
344 were stretched at 5 pN force, preventing DNA condensation. To allow DNA condensation by
345 bound $ParB_F$ molecules, the force was dropped to 0.05 pN and the tether extension was monitored
346 for 30 sec. To assess the stability of DNA condensation by $ParB_F$ dimers, tether extension was
347 monitored after increasing the force to 5 pN. In the absence of CTP, we only observed
348 condensation at very high concentrations of $ParB_F$ (>5 μM) and did not see a significant difference
349 between $parS_F$-containing and non-specific tethers (Figure 6B inset). However, in the presence of
350 CTP, 50 nM $ParB_F$ robustly condensed $parS_F$-containing DNA tethers (Figure 6B purple). These
351 condensed protein-DNA complexes resisted 5 pN extension force, requiring many minutes at 5 pN
352 tension to de-condense (Figure 6—figure supplement 1A). The slow de-condensation took place

353 through a series of abrupt steps, which we interpret as stepwise opening of large DNA loops held
354 by multiple $ParB_F$—$ParB_F$ interactions (Figure 6—figure supplement 1A). Condensation was
355 comparable for DNA molecules that were topologically constrained, i.e., could be supercoiled, or
356 unconstrained (nicked), suggesting that condensation is not a consequence of topological changes
357 in the DNA caused by $ParB_F$ translocating away from $parS_F$ sites (Figure 6—figure supplement 2).
358 We observed some condensation events with $parS_F$ containing tethers in the presence of CDP, but
359 these events were rarer, required higher $ParB_F$ concentrations, and were almost completely de-
360 condensed within 5 sec of raising the force to 5 pN, in stark contrast to condensation in the presence
361 of CTP (Figure 6B light blue, Figure 6—figure supplement 1B). Since this experiment was also
362 carried out using CDP that contained a compound hydrolysable by $ParB_F$, contribution of this
363 compound to the limited tether condensation cannot be ruled out. In contrast, $ParB_F$ was unable
364 to substantially condense DNA tethers lacking $parS_F$ sequences, even in the presence of CTP, and
365 rare condensation events were quickly reversed by the application of 5 pN force (Figure 6B dark
366 blue). Addition of $parS_F$-containing DNA fragments together with $ParB_F$ and CTP did not rescue
367 the inability to condense tethers lacking $parS_F$, indicating that $parS_F$ cannot act *in trans* to promote
368 ParB spreading and condensation of DNA molecules (Figure 6—figure supplement 3). Together
369 these results indicate that $parS_F$ mediates loading of multiple CTP-bound $ParB_F$ dimers *in cis* onto
370 the DNA-tethers and these $ParB_F$ dimers are capable of forming DNA looping bridges likely *via*
371 inter-dimer interactions to form a condensed partition complex-like structure. As expected,
372 $ParB_F^{R121A}$ bearing a mutation at the critical Box II residue in the CTPase domain was unable to
373 condense DNA to a significant degree even with $parS_F$ containing tethers (Figure 6B red). We

374 propose that stable DNA condensation by $ParB_F$ is mediated by CTPase domain dimerization and
375 requires both *$parS_F$* and CTP at moderate $ParB_F$ concentrations (~100 nM) (Figure 6C).

376

377 **Discussion**

378 In this report, we characterized facets of the $ParA_F$—$ParB_F$ interaction leading to the assembly of
379 the nsDNA-bound $ParA_F$—$ParB_F$ complex that is required to activate $ParA_F$ for ATP hydrolysis
380 and dissociation from nsDNA under the influences of *$parS_F$* and CTP (Summarized in Figure 7).
381 Our results indicate that both $ParB_F$ binding faces of the nsDNA-bound $ParA_F$ dimers must be
382 occupied by a $ParB_F$ N-terminal domain for ATPase activation (Figure 2C-G and 7B). In principle,
383 two copies of the $ParB_F$ N-terminal domain activating a $ParA_F$ dimer could belong to one $ParB_F$
384 dimer as seen in the absence of CTP or *$parS_F$* (Figure 4A-B and 7B middle). However, most $ParB_F$
385 dimers in partition complexes *in vivo* are likely in the CTP- and *$parS_F$*-activated state, spreading
386 over a *$parS_F$*-proximal DNA region. CTP or *$parS_F$* binding alters the $ParB_F$ dimer structure to
387 prevent a single $ParB_F$ dimer from providing both copies of the N-terminal domain to occupy both
388 binding faces of a $ParA_F$ dimer, necessitating two $ParB_F$ dimers, each providing one N-terminal
389 domain to a $ParA_F$ dimer (Figure 4C-D, Figure 5 and Figure 7B bottom). Strikingly, *$parS_F$* together
390 with CTP significantly increased the A_2B_4 complex assembly rate on nsDNA without strongly
391 affecting its disassembly rate. Although we have not analyzed the full kinetic details of the process
392 that leads to ATPase activation by $ParB_F$, we propose that a moderately slow transition separates
393 formation of the ATPase-activated A_2B_4 complex from the rapidly reversible $ParA_F$—$ParB_F$
394 interaction processes. Such a local slow step would partially decouple the reversible $ParA_F$—$ParB_F$
395 interaction dynamics from the irreversible ATP hydrolysis, thereby promoting dynamic

396 interactions between the nucleoid and partition complex that facilitate partitioning *via* the
397 diffusion-ratchet mechanism as elaborated below.

398 The clearest indication that both $ParB_F$-interacting faces of the nsDNA-bound $ParA_F$ dimer must
399 be occupied by the N-terminal domain of $ParB_F$ for ATPase activation came from experiments
400 using artificial $ParB_F$ constructs. We showed that monomeric $ParB_F^{1-42}$ stimulates $ParA_F$ ATPase
401 with a clear sigmoidal concentration dependence, indicating that one molecule of $ParB_F^{1-42}$ binding
402 to one side of a $ParA_F$ dimer cannot fully activate the $ParA_F$ ATPase (Figure 2F). When ATP
403 hydrolysis was blocked by using non-hydrolysable ATPγS, $ParB_F^{1-42}$-mCherry formed an
404 equimolar complex with $ParA_F$ (Figure 2C-E). Thus, the $ParA_F$ forms a complex with $ParB_F^{1-42}$-
405 mCherry bound at both $ParB_F$-interacting faces of the $ParA_F$ dimer prior to ATP hydrolysis (Fig
406 7B; top). Consistently, an artificially dimeric $ParB_F^{1-42}$ construct, $ParB_F^{1-42}$-mCherry-EcoRI^{E111Q},
407 efficiently activated $ParA_F$-ATPase with hyperbolic concentration dependence (Figure 2G).

408 In the absence of CTP or $parS_F$, the $ParB_F$ dimer is held together by the C-terminal self-
409 dimerization domain (Fig 7A bottom) with dimerization K_D of ~19 nM (Figure 4—figure
410 supplement 1). In this state, the N-terminal halves of the monomers are thought to be separate from
411 each other according to the SAXS envelope of the structure (Chen et al., 2015; also see Figure 2—
412 figure supplement 3B). Thus, one dimer could straddle a $ParA_F$-dimer with each N-terminal $ParA_F$-
413 interaction domain interacting with one of the two faces of a $ParA_F$-dimer (Figure 7B middle).

414 In contrast, when bound by CTP the CTPase domains in a $ParB_F$ dimer fold to form a single
415 globular domain (Figure 7A bottom) (Soh et al., 2019; see Figure 2—figure supplement 3C). The
416 two $ParA_F$-interaction domains emanating from this dimeric domain are unlikely to reach both

417 sides of a $ParA_F$ dimer, necessitating an A_2B_4 complex for ATPase activation (Figure 7B bottom).
418 In theory, it is possible that a chain of $(A_2B_2)_n$ might form, but the 1:2 protein stoichiometry
419 observed in the presence of ATPγS indicates such a configuration is unfavored. A_2B_4 complexes
420 formed in the presence of CTP and *parS*$_F$ DNA fragments contained almost no *parS*$_F$ DNA
421 fragments (Figure 5D). This is consistent with the notion that after binding *parS*$_F$, CTP-$ParB_F$
422 dimers convert to a low *parS*$_F$-affinity state while remaining topologically bound to the DNA and
423 spreading to surrounding DNA regions (Soh et al., 2019). The A_2B_4 complex formed in the
424 presence of *parS*$_F$ DNA fragments, even without CTP, contained significantly less than a
425 stoichiometric amount of *parS*$_F$ fragment (Figure 5D). This suggests that association with nsDNA-
426 bound $ParA_F$ dimer lowers the affinity of $ParB_F$ for *parS*$_F$, perhaps shifting the structure closer
427 toward *parS*$_F$-activated $ParB_F$-CTP.

428 The ParB : ParA stoichiometry change from 1:1 to 2:1 caused by *parS*$_F$ (Figure 4C, D) did not
429 occur with the Box II mutant $ParB_F^{R121A}$ (Figure 4—figure supplement 2). It is possible that when
430 a $ParB_F$ dimer binds *parS*$_F$, the adjacent CTPase domains of the two monomers adopt a mutually
431 interacting folded state akin to the CTP-bound state even without CTP, promoting a BoxII-
432 dependent dimerized domain structure. This may disfavor formation of the A_2B_2 complex, favoring
433 the A_2B_4 complex that was observed.

434 All the A_2B_2 and A_2B_4 complexes we observed in the presence of ATPγS dissociated from nsDNA
435 more slowly (k_{off} = 0.5 - 1 min^{-1}; Supplementary Table 1) compared to $ParA_F$ in the absence of
436 $ParB_F$ (~6 min^{-1}; Fig 2B). For the case of monomeric $ParB_F^{1-42}$, which dissociated from $ParA_F$ more
437 rapidly, the presence of 10 μM $ParB_F^{1-42}$ in the wash buffer restored the low apparent nsDNA

438 dissociation rate constant of the complex (Figure 2E). Nevertheless, $ParA_F$ dimers in these
439 complexes appear to be primed for further conformational change toward less stably DNA-
440 associated state. Upon dissociation of $ParB_F^{1-42}$ from the $A_2B^{1-42}{}_2$ complex, $ParA_F$ dissociated from
441 the DNA-carpet within a second or so, much faster than the ATPγS-$ParA_F$-dimer that has not yet
442 formed a A_2B_2 or A_2B_4 complex (Figure 2D, 3B).

443 Our single-molecule DNA condensation measurements indicate that CTP-bound $ParB_F$ dimers are
444 activated by contacting *parS*$_F$ to load *in cis* onto the *parS*$_F$-carrying DNA in numbers exceeding
445 the copy number of the *parS*$_F$-consensus sequence (ParB spreading) as shown by others for
446 chromosomal ParBs (Jalal et al., 2020; Soh et al., 2019), and condense the DNA forming an *in*
447 *vivo* partition complex-like structure (Figure 6). Although the magnetic tweezers instrument used
448 in this study did not allow direct measurement of the number of $ParB_F$ molecules contained in the
449 condensed DNA, the large number of de-condensation steps observed when high tension was
450 applied is consistent with the presence of a large number of $ParB_F$ dimers in the condensed DNA
451 (Figure 6, Figure 6—figure supplement 1A). CDP failed to support efficient condensation of
452 *parS*$_F$-carrying DNA by $ParB_F$ and the limited condensation observed, which could be due to the
453 contaminating material in the CDP used, was disrupted far more readily than CTP-supported
454 condensates (Figure 6, Figure 6—figure supplement 1B). Our results show that DNA-condensation
455 is caused by $ParB_F$—$ParB_F$ interactions forming DNA-looping bridges without requiring other
456 protein factors. Combined with evidence indicating that *parS*$_F$-activated $ParB_F$—CTP adopts a
457 unique conformational state (Soh et al., 2019), we favor the view that DNA-bridging capability,
458 mediated by inter-dimer $ParB_F$ interaction, is another attribute of this $ParB_F$ state.

459 Our observation indicates that the state of $ParB_F$ discussed above is maintained after release from
460 *$parS_F$*-containing DNA. $ParB_F$ associates with nsDNA-bound $ParA_F$ dimers forming the A_2B_4
461 complex with a faster apparent assembly rate in the presence of *$parS_F$* and CTP together than with
462 either CTP or *$parS_F$* alone. This observation is consistent with the decreased half-saturation
463 concentration in the ATPase activation assay (Figure 5F, Table 2). According to the sliding clamp
464 model of spreading ParB—CTP dimers proposed by Soh et al., (2019), $ParB_F$—CTP dimers loaded
465 onto a short *$parS_F$* DNA fragments would quickly slide off the DNA as shown by Jalal et al., (2020).
466 Since our ATPase activation assay and the DNA-carpet-bound A_2B_4 complex assay in the presence
467 of CTP and *$parS_F$* were done using a short linear *$parS_F$* DNA fragment, the *$parS_F$*-activated state
468 of the $ParB_F$—CTP dimers we described in this study must remain in this "activated" state for an
469 extended period after sliding off the *$parS_F$* fragment. Accordingly, the A_2B_4 complexes bound to
470 the DNA-carpet in the presence of CTP, ATPγS and *$parS_F$* fragments contained almost no *$parS_F$*
471 fragments (Figure 5D). Thus, *$parS_F$* acts as a catalyst to convert $ParB_F$—CTP dimers from a pre-
472 activation state to an activated state capable of faster A_2B_4 complex assembly. This notion is also
473 consistent with the observation that significantly less than a stoichiometric concentration of *parS*
474 DNA relative to ParB is sufficient for full activation of the ParB CTPase (Figure 5—figure
475 supplement 2C; Soh et al., 2019). Although the $ParB_F$ dimers in this activated state failed to load
476 efficiently onto DNA lacking *$parS_F$* sequences *in trans* (Figure 6—figure supplement 3), in the
477 absence of contrary evidence, the parsimonious assumption is that this $ParB_F$ dimer retains the
478 conformation of spreading $ParB_F$ dimers that remain loaded on the *$parS_F$*-containing DNA *in cis*.
479 Thus, we propose that the functional properties of $ParB_F$ we observed in the presence of CTP and

480 *parS*$_F$, both in facilitating assembly of A_2B_4 complexes and activating ParA$_F$-ATPase, reflect those
481 of the majority of ParB$_F$ dimers in partition complexes *in vivo*.

482 Our study, together with previous studies, indicates that the ATP turnover rates of ParABS systems
483 are slow because of multiple, slow kinetic steps. These slow steps are strategically placed in the
484 reaction pathway in order to tune the system and drive the motion of the partition complex through
485 the diffusion-ratchet mechanism (Sugawara and Kaneko, 2011; Vecchiarelli et al., 2010). Even at
486 saturating concentrations of ParB$_F$ in the *parS*$_F$-activated CTP-bound state, the maximum ATP
487 turnover rate of ParA$_F$ remained modest (~80 ATP/ParA$_F$-monomer/hour; Figure 5). The slow
488 reactivation of ParA nucleoid binding after ATP hydrolysis likely dominates the overall ATPase
489 cycle time (Vecchiarelli et al., 2010). The presence of a large fraction of ParA$_F$ in DNA-unbound
490 state during the steady state ATPase assay was evidenced by the fact that the half-saturation
491 concentration of ParB$_F$ (in the presence of CTP and *parS*$_F$) forming the A_2B_4 complex was ~0.2
492 μM while the total ParA$_F$ concentration was 1 μM, suggesting less than ~20% of ParA$_F$ was in the
493 nsDNA-bound state ready to interact with ParB$_F$. *In vivo* the reactivation rate is likely lower since
494 nucleoid-bound ParA is only fully activated on encountering the partition complex, which lowers
495 the concentration of ParA in the cytosol waiting to be reactivated. The lower precursor
496 concentration slows the nucleoid rebinding rate of ParA non-linearly because reactivation involves
497 a relatively fast nucleotide-dependent reversible ParA dimerization with apparent K_D of ~2 μM,
498 followed by a slow conformational step. This makes the process dimerization-limited at lower
499 precursor ParA concentrations according to the study of ParA$_{P1}$ (Vecchiarelli, 2010). Whereas this
500 slow ParA reactivation and rebinding process, which allows the maintenance of the nucleoid-
501 bound ParA concentration gradient (Hu et al., 2017), is a critical element of chemophoresis driven

motility, the rate of ParA-ATPase activation by ParB is another important factor. In particular, efficient chemophoresis force generation relies on $ParA_F$—$ParB_F$ interactions achieving a local quasi-equilibrium prior to ATP hydrolysis (Sugawara and Kaneko, 2011). Therefore, we speculate that there is a significant energy barrier associated with the conformational transition of a $ParA_F$—$ParB_F$ complex to achieve ATPase activation (Figure 7C). The resulting local time delay, in addition to the fact that two ParB dimers are required to bind a ParA dimer to activate its ATPase, would partially decouple the pre-ATP hydrolysis $ParA_F$—$ParB_F$ reversible interaction steps from the ATP hydrolysis step. This delay would in turn permit ParB—ParA binding to approach local quasi-equilibrium, increasing the efficiency of ParA distribution gradient sensing and motive force generation by the partition complex. In addition, this slow activation step would prevent possible over-depletion of the local nucleoid-bound $ParA_F$ as the partition complex establishes the $ParA_F$ depletion zone.

Disassembly of the ATP-bound A_2B_4 complex might be slow prior to ATP hydrolysis considering the stability of the complexes in the presence of ATPγS. Thus, we propose the energy barrier postulated above is positioned immediately prior to formation of this complex rather than between this complex assembly and ATP hydrolysis. A slow step after formation of the stable complex would prolong the lifetime of the link between the nucleoid and the partition complex impeding partition complex motion without permitting the reversible $ParA_F$—$ParB_F$ interaction to approach equilibrium. We consider this conformational transition is likely the step synergistically accelerated by CTP and $parS_F$. We note that CTP-activated $ParB_F$ stimulates $ParA_F$ ATPase with sigmoidal concentration dependence (Figure 5E-F, Table 2) suggesting two $ParB_F$ dimers separately bind a $ParA_F$ dimer during a pre-equilibrium binding phase, forming a transient $B_2A_2B_2$

524 complex. We imagine the slow conformational step proposed here might be assisted by the
525 property of the CTP/*parS*$_F$-activated ParB$_F$ dimers that promotes inter-dimer interactions as
526 suggested by the magnetic tweezers experiments, stabilizing the interaction between the two ParB$_F$
527 dimers within a complex, depicted as conversion of $B_2A_2B_2$ complex to A_2B_4 complex in Figure
528 7C. This might explain the higher assembly rate and stability of the complex formed with *parS*$_F$-
529 activated ParB$_F$-CTP. Yet, CTP and *parS*$_F$ DNA do not significantly increase the ATP turnover
530 rate of ~80 h^{-1}, indicating that the proposed kinetic delay time must be a small fraction of the
531 ATPase cycle time (~45 sec), for which we believe the rate limiting step resides in the reactivation
532 process of ParA for nsDNA binding after ATP hydrolysis (Vecchiarelli et al., 2010). Assembly of
533 the $A_2B^{1\text{-}42}{}_2$ complex perhaps does not experience this time delay due to fewer steric constraints,
534 but ParB$_F^{1\text{-}42}$ dissociates more readily compared to full-length ParB$_F$. If two CTP-bound and parS$_F$-
535 activated ParB$_F$ dimers independently associating with a nucleoid-bound ParA$_F$-ATP dimer is
536 important for efficient partition complex motive force generation by the chemophoretic principle
537 as proposed above, one might be able to design a mutant ParB$_F$ that can activate ParA$_F$-ATPase by
538 forming an A_2B_2 complex even in the presence of CTP, which would significantly affect plasmid
539 partition efficiency. Efforts to generate such ParB$_F$ mutants are currently under way.

540 This study demonstrates how *parS*$_F$, along with CTP, has wide-reaching roles in the F-plasmid
541 ParABS system; not only in ParB$_F$'s ability to spread from *parS*$_F$ and promote ParB$_F$—ParB$_F$
542 interactions for partition complex compaction, but also in ParB$_F$ dimer interactions with ParA$_F$.
543 However, we still need to investigate how the ParB$_F$ CTPase activity is impacted by *parS*$_F$ in
544 different states of the ParB$_F$—*parS*$_F$ complex and its interaction with the ParA$_F$-DNA complex.
545 More generally, in order to understand how the system is orchestrated to achieve system dynamics

546 that result in robust plasmid segregation, improved understanding of the microscopic kinetic
547 parameters is essential. Many details of the system dynamics still remain to be addressed to
548 understand the full picture of the ParABS partition mechanism.

549 **Materials and Methods**

550

Key Resources Table				
Reagent type (species) or resource	**Designation**	**Source or reference**	**Identifiers**	**Additional information**
strain, strain background (*Escherichia coli*)	BL21 DE3 AI	Invitrogen	C607003	protein expression strain
recombinant DNA reagent	pET11a	EMD Millipore	9436	protein expression vector
recombinant DNA reagent	pET28a-*parS*$_F$	This work		tether DNA PCR template
recombinant DNA reagent	pET28a	EMD Millipore	69865	tether DNA PCR template
recombinant DNA reagent	pBlueScript II KS(+)	Agilent	212207	tether DNA PCR template
recombinant DNA reagent	pX7	Vecchiarelli et al., 2013		ParA$_F$ overexpression plasmid
recombinant DNA reagent	pX2	Vecchiarelli et al., 2013		ParA$_F$-eGFP overexpression plasmid
recombinant DNA reagent	pX8	Vecchiarelli et al., 2013		ParB$_F$ overexpression plasmid
recombinant DNA reagent	pET11a-ParB$_F^{R121A}$	This work		ParB$_F^{R121}$ overexpression plasmid

recombinant DNA reagent	pET11a-$ParB_F^{1-42}$-mCherry	This work		$ParB_F^{1-42}$-mCherry overexpression plasmid
recombinant DNA reagent	pET11a-$ParB_F^{1-42\ R36A}$-mCherry	This work		$ParB_F^{1-42\ R36A}$-mCherry overexpression plasmid
recombinant DNA reagent	pET11a-$ParB_F^{1-42}$-mCherry-$EcoRI^{E111Q}$	This work		$ParB_F^{1-42}$-mCherry-$EcoRI^{E111Q}$ overexpression plasmid
sequence-based reagent	*$parS_F$* DNA	This work		5'-AGTCTGGGACCACGGTCCCACTCG
sequenced-based reagent	*$parS_F$* DNA Alexa 488	This work		5'-Alexa488-(HNS)-AGTCTGGGACCACGGTCCCACTCG
sequenced-based reagent	*$parS_F$* DNA complement strand	This work		5'-CGAGTGGGACCGTGGTCCCAGACT
sequence-based reagent	Scrambled seq DNA	This work		5'-AGTCTGCAGCTACTATACCACTCG
sequence-based reagent	Scrambled seq DNA complement strand	This work		5'-CGAGTGGTATAGTAGCTGCAGACT
sequence-based reagent	EcoR1 sequence + strand	This work		5'-GAATTCCGAGTGGGACCGTGGTCCCAGTCTGATTATCAGACCGAGAATTCAAGTTGGGACCGTGGTCCCAAGAGAAT
sequence-based reagent	EcoR1 sequence - strand	This work		5’-ATTCTCTTGGGACCACGGTCCCAACTTGAATTCTCGGTCTGATAATCAGACTGG

				GACCACGGTCCCA CTCGGAATTC
sequence-based reagent	5kb DNA primer1	Seol et al., 2011		5'-GCTGGGTCTCGGTT GTTCCCTTTAGTGA GGGTTAATTG
sequence-based reagent	5kb DNA primer2	Seol et al., 2011		5'-GCTGGGTCTCGTG GTTTCCCTTTAGTG AGGGTTAATTG
sequence-based reagent	DNA handle primer1	Seol et al., 2011		5'-GGACCTGCTTTCGT TGTGGCGTAATCAT GGTCATAG
sequence-based reagent	DNA handle primer2	Seol et al., 2011		5'-GGGTCTCGTGGTTT ATAGTCCTGTCGG GTTTC
peptide, recombinant protein	$ParB_F^{1-42}$	This work		MKRAPVIPKHTLNT QPVEDTSLSTPAAP MVDSLIARVGVMA R
peptide, recombinant protein	$ParB_F^{1-42\ R36A}$	This work		MKRAPVIPKHTLNT QPVEDTSLSTPAAP MVDSLIAAVGVMA R
chemical compound, drug	ATP	Millipore-Sigma	A2383	
chemical compound, drug	GTP	Millipore-Sigma	G8877	
chemical compound, drug	UTP	Thermo Scientific	J23160	
chemical compound, drug	CTP	Millipore-Sigma	C1506	

chemical compound, drug	CDP	Millipore-Sigma	C9755	2-3% possible contamination of $ParB_F$-CTPase substrate detected
chemical compound, drug	γ^{32}P-ATP	Perkin-Elmer	NEG002A250UC	
chemical compound, drug	Dynabeads™ MyOne™ Streptavidin T1	Invitrogen	65601	
chemical compound, drug	Alexa Fluor 488 C5 Maleimide	Thermo Fisher	A10254	
chemical compound, drug	Alexa Fluor 594 C5 Maleimide	Thermo Fisher	A10256	
chemical compound, drug	Alexa Fluor 647 C2 Maleimide	Thermo Fisher	A20347	
chemical compound, drug	Antifoam Y-40 emulsion	Sigma	A5758	
chemical compound, drug	EDTA-free Sigmafast protease inhibitor cocktail tablet	Sigma	S8830	
chemical compound, drug	DOPC	Avanti polar lipids	850375C	
chemical compound, drug	DOPE-Biotin	Avanti polar lipids	850149P	
chemical compound, drug	Biotin-14-dCTP	Thermo Fisher	19518018	
chemical compound, drug	Biotin-16-dUTP	Roche	11093070910	
chemical compound, drug	Digoxigenin-11-dUTP	Roche	11093088910	

commercial assay or kit	EnzCeck Phosphate assay kit	Thermo Fisher	E6646	
software, algorithm	Prism 8	GraphPad	Prism 8	Used for curve fitting, and fitting parameters and their error estimation.
software, algorithm	Igro Pro 7	Wavemetrics	Igro Pro	Used for single molecule data analysis.
software, algorithm	LabVIEW	National Instruments	LabView NXG Full	Used for instrumental control in single molecule experiments.
software, algorithm	Metamorph 7	Molecular Devices	Metamorph 7	Used for TIRF michroscope data acquisition.
software, algorithm	ImageJ/Fiji	National Institutes of Health	ImageJ	Used for TIRF michroscope image analysis.
other (Instrument)	Prism type TIRF microscope	In house	Ivanov & Mizuuchi, 2010; Vecchiarelli et al., 2013	Used for ParAF-ParBF complex assembly-disassembly experiments.
other (Instrument)	Magnetic tweezers	In house	Seol et al., 2011 and 2016	Used for taking single molecule measurements of enzyme binding on 5kb DNA.
other (Instrument)	Plate reader	BMG Labtech	Clariostar Plus	Used for FRET-based ParBF dimerization K_D and CTP hydrolysis assays using EnxCheck Phosphate assay kit

551

552 *Plasmids and constructs for protein expression*

553 All expression open reading frames were synthesized and subcloned into pET11a (Genscript).
554 $ParA_F$, $ParA_F$-eGFP, $ParB_F$, $ParB_F^{R121}$, $ParB_F^{1-42}$-mCherry, $ParB_F^{1-42\ R36A}$-mCherry and $ParB_F^{1-42}$-
555 mCherry-$EcoRI^{E111Q}$ constructs were made with a hexa-histidine tag on their C-terminus. Protein
556 fusions were made with a SGGG linker between fused domains, with exception of $ParB_F^{1-42}$-
557 mCherry-$EcoRI^{E111Q}$ which had a 4x (SGGG) linker between $ParB_F^{1-42}$ and mCherry. $ParB_F^{1-42}$ and
558 $ParB_F^{1-42\ R36A}$ were synthesized *de novo* (Genscript).

559 *Oligonucleotides*

560 The 24 bp double-stranded DNA fragments containing the $parS_F$ consensus sequence and a
561 scrambled sequence used in this study were: 5'-AGT CTG GGA CCA CGG TCC CAC TCG; 5' -
562 AGT CTG CAG CTA CTA TAC CAC TCG, respectively and their complements. The
563 fluorescently labelled $parS_F$ substrate was synthesized with Alexa-488 NHS coupled to the 5' of
564 the forward strand by the manufacturer (IDT).

565 *Protein purification and fluorescent labelling*

566 For expression of proteins 5 ml of an overnight culture of BL21 DE3 AI (Invitrogen) *E. coli* cells
567 transformed with the desired plasmid were inoculated into 500 ml Terrific Broth (Teknova)
568 supplemented with 100 µg/ml carbenicillin, antifoam Y-40 emulsion (Sigma), 1 g/l NaCl, 0.7 g/l
569 Na_2SO_4, 2.6 g/l NH_4Cl, and 0.24 g/l $MgSO_4$. The cultures were incubated at 37 °C in 2.5 l Fernbach
570 flasks and shaken at 120 rpm until they reached an OD_{600} of 1.8. Cultures were chilled on ice before
571 they were induced by the addition of 1 mM IPTG and 0.2 % L-arabinose. Following induction,

572 cultures were incubated at 16 °C for 16 hr and cells were harvested by centrifugation at 6000 x g
573 for 15 min at 4 °C. Cell pellets were frozen in liquid nitrogen and stored at -80 °C.

574 Frozen cells were thawed and resuspended to a density of 1 g cell pellet/10 ml in lysis buffer
575 ($ParA_F$, $ParA_F$-eGFP and $ParB_F^{1-42}$-mCherry-EcoRI^{E111Q}: 25 mM Tris.HCl pH 8, 1 M NaCl, 20 mM
576 imidazole, 2 mM β-mercaptoethanol, 10% glycerol; $ParB_F$ and $ParB_F^{R121A}$: 10 mM Sodium
577 Phosphate buffer pH 7, 1 M NaCl, 20 mM Imidazole , 2 mM β-mercaptoethanol, 10% glycerol;
578 $ParB_F^{1-42}$-mCherry and $ParB_F^{1-42/R36A}$-mCherry: 25 mM HEPES.KOH pH 7.5, 150 mM NaCl, 6 M
579 guanidinium chloride, 20 mM Imidazole, 2 mM β-mercaptoethanol, 10% glycerol) containing
580 EDTA-free Sigmafast protease inhibitor cocktail tablet (Sigma) using a homogenizer. Lysozyme
581 and Benzonase (Sigma) were added to a concentration of 1 mg/ml and 50 u/ml, respectively, and
582 the cells were lysed *via* a microfluidizer. Cell debris were pelleted by centrifugation at 142,000 x
583 g for 45 min at 4 °C, and the supernatant passed through a 0.22 μm filter.

584 Lysate was loaded on to a 5 ml HisTrap HP cassette (GE Healthcare) equilibrated in lysis buffer.
585 The cassette was then washed with 10 column volumes of lysis buffer followed by 10 column
586 volumes HisTrap buffer (as lysis buffer without guanidinium hydrochloride and with the following
587 NaCl concentrations: $ParA_F$ proteins, 200 mM; $ParB_F$ proteins, 150 mM), and the protein eluted
588 with a gradient from 20 to 500 mM imidazole over 10 column volumes using an AKTA Pure (GE
589 Healthcare).

590 All proteins except $ParB_F^{1-42}$-mCherry and $ParB_F^{1-42\ R36A}$-mCherry were then subjected to ion-
591 exchange chromatography. The peak fractions from the HisTrap column were pooled and slowly
592 diluted whilst stirring with a Mono Q/S-buffer (as lysis buffer without imidazole or NaCl, but with

593 0.1 mM EDTA pH 8) until the conductivity of the sample was: 18 mS/cm for $ParA_F$ proteins, 5
594 mS/cm for $ParB_F^{1-42}$-mCherry-$EcoRI^{E111Q}$ and 15 mS/cm for all other $ParB_F$ proteins. The
595 conductivity of the samples was monitored using a conductivity meter (Hanna). The sample was
596 loaded onto either a 1-ml Mono Q ($ParA_F$ proteins and $ParB_F^{1-42}$-mCherry-$EcoRI^{E111Q}$) or Mono S
597 (other $ParB_F$ proteins) 5/50 GL ion exchange column (GE Healthcare) pre-equilibrated with Mono
598 Q/S-buffer containing a NaCl concentration to match the conductivity of the sample. The column
599 was then washed with 10 column volumes of Mono Q/S-buffer + NaCl. The protein was eluted
600 with a gradient up to 500 mM NaCl over 10 column volumes.

601 Finally, all protein samples were purified by size-exclusion chromatography. The peak fractions
602 from the previous column were pooled and diluted 50:50 with concentration buffer (25 mM
603 HEPES.KOH pH 7.5, 2 M NaCl, 2 mM β-mercaptoethanol, 10% glycerol) and concentrated to ~2
604 ml using a Centriprep 10-kDa spin concentrator (Millipore). The sample was then injected onto an
605 S200 16/600 size exclusion column (GE Healthcare) pre-equilibrated in gel filtration buffer (25
606 mM HEPES-KOH pH 7.5, 0.1 mM EDTA pH 8, 0.5 mM TCEP and 10% glycerol with 600 mM
607 KCl for $ParA_F$ proteins and 150 mM KCl for $ParB_F$ proteins). Peak fractions were then pooled and
608 concentrated to ~100 μM (~5-10 mg/ml) as determined by UV 280 nm absorbance before being
609 aliquoted, frozen in liquid nitrogen and stored at –80 °C. Protein aliquots were used once and not
610 subjected to freeze-thaw cycles.

611 To produce fluorescently labeled $ParB_F$ and $ParB_F^{R121A}$, $ParB_F$ protein was buffer exchanged into
612 gel filtration buffer without reducing agent and incubated with a two-fold molar excess of Alexa
613 Fluor 647 C2 Maleimide (Thermo Fisher) for 30 min at room temperature. The reaction was then

614 quenched by the addition of DTT to a final concentration of 10 mM. The protein solution was then
615 filtered through a 0.22 μm filter and free dye removed by buffer exchange into gel filtration buffer
616 in Amicon ultra 10 kDa spin concentrator (Millipore). The extent of labeling was estimated based
617 on absorbance at 280 and 647 nm.

618 *Assaying contaminating activities in the protein preparations*

619 Proteins purified by the above protocol had no significant DNA endonuclease activity. After 16 hr
620 incubation of supercoiled pBR322 with 2 μM $ParA_F$ and/or 10 μM $ParB_F$ at 37 °C in ATPase buffer
621 (see below) no linear DNA was observed and less than 10% of the supercoiled plasmid was
622 converted to a nicked-circular form. The contaminating ATPase activity for all $ParB_F$ proteins was
623 less than two mol ATP per mol $ParB_F$ per hour, as determined by the ATPase assay protocol
624 detailed below.

625 *ATPase activity assays*

626 Steady-state ATPase activity was measured as described (Vecchiarelli et al., 2016) with
627 modifications. ATP to be used for ATPase activity assays was purified after diluting 20 μCi ATP
628 γ-P^{32} (Perkin-Elmer) in 100 μl of 100 mM unlabeled ATP (Sigma) by passing through a 3 ml P2
629 resin size-exclusion column equilibrated with a buffer containing 50 mM HEPES·KOH pH 7.5,
630 150 mM KCl and 0.1 mM EDTA. The purity of fractions was determined by TLC. 1 μl of each
631 fraction was spotted on to a 10 x 8 cm piece of TLC PEI Cellulose F paper (Millipore) 1 cm above
632 the bottom of the paper and developed for 10 mins using 400 mM NaH_2PO_4 pH 3.6 as the solvent.

633 The fractions containing the minimum contamination of P^{32}-Pi were pooled and their concentration
634 determined by spectrometry before storage at -20 °C.

635 $ParA_F$ ATPase activity was measured in the presence of the combinations and concentrations of
636 proteins and DNA cofactors specified in the main text in ATPase buffer (50 mM HEPES·KOH pH
637 7.5, 150 mM KCl, 5 mM $MgCl_2$, 0.5 mM TCEP and 1 mM ATP γ-P^{32}). Reactions were incubated
638 at 37 ºC for 4 hrs and stopped by the addition of an equal volume of 1 M formic acid. The increase
639 of P^{32}-Pi was measured by TLC using PEI Cellulose F paper as detailed above.

640 *$ParB_F$ NTPase activity assays*

641 Steady state $ParB_F$ CTPase activity was measured in CTPase buffer containing 50 mM Tris-HCl
642 pH 7.5, 100 mM NaCl, 2 mM $MgCl_2$, 1 mM DTT, 100 μg/ml BSA, 200 μM MESG (EnzChek
643 probe), 1 U/ml of purine nucleotide phosphorylase, and $ParB_F$, *$parS_F$* DNA and CTP at
644 concentrations specified in the figure, following the protocol of the supplier of the EnzChek
645 phosphate assay kit (ThermoFisher). Reactions were typically repeated three times using 96-well
646 microtiter plates and the 360 nm absorption signal increase was monitored at half to one min
647 intervals using Clariostar Plus plate reader (BMG Labtech). The absorption signal increase after
648 subtraction of background time course in the absence of enzyme was converted to released Pi
649 concentration increase based on phosphate titration measurements. The CTP hydrolysis rate was
650 calculated from the initial slope of the time course curve, which typically started after ~7 min
651 deadtime for the plate setting up. Substrate specificity was examined comparing Pi release from
652 four ribonucleoside triphosphates. Attempt to examine inhibition of the CTPase activity by CDP
653 or to detect CDP binding to $ParB_F$ was postponed when the CDP used in this study was found to

654 release Pi upon incubation with $ParB_F$. CDP obtained from two additional suppliers also generated
655 similar quantities of Pi upon incubation with $ParB_F$.

656 *TIRF microscopy*.

657 The general design of the TIRF microscopy setup was essentially as previously described (Ivanov
658 and Mizuuchi, 2010; Vecchiarelli et al., 2013). A prism-type TIRFM system was built around an
659 Eclipse Ti microscope (Nikon) with a 40x objective (S Fluor, 40x/1.30 oil, Nikon) and two-color
660 images captured by an Andor DU-897E camera through a dxcr630 insert DualView (Photometrics)
661 with the following settings: 3 MHz digitizer (grey-scale); 5.2 pre-amplifier gain, 2 MHz vertical
662 shift speed; +1 vertical clock range; electron-multiplying gain 30; EM CCD temperature set at -90
663 ºC; baseline clamp ON; and exposure time 100 ms.

664 The excitation for $ParA_F$-eGFP and Alexa647-$ParB_F$ were provided by a 488 nm diode-pumped
665 solid-state laser (Sapphire, Coherent) and a 633 nM HeNe laser (Research Electro-Optics),
666 respectively. The TIRF illumination had an elliptical Gaussian shape in the field of view therefore
667 intensity data for DNA-carpet-bound $ParA_F$-eGFP and Alexa647-$ParB_F$ signals were taken at or
668 near the middle of the illumination profile.

669 Movies were acquired using Metamorph 7 (Molecular Devices) and transferred to ImageJ
670 (National Institutes of Health) for analysis.

671 Flow cells were assembled using fused silica microscope slides with pre-drilled inlet/outlet ports
672 (Esco products), #1 glass cover slips (24 x 50 mm, Thermo Fisher) and 0.001”-thick acrylic
673 transfer tape (3M). The fused silica slide was cleaned by soaking overnight in a solution of

674 Nochromix (Sigma)-sulfuric acid, followed by extensive rinsing with de-ionized water, drying by
675 blowing nitrogen gas, followed by oxygen plasma treatment (South Bay Technology Inc). The Y-
676 shaped flow path pattern was cut out of the transfer tape using a laser cutter before the flow cell
677 assembly. Nanoports (Idex) were attached to the fused silica slide for the inlet and outlet tube
678 connections using Norland Optical Adhesive (Thorlabs), cured by 365 nm UV light. The
679 assembled flow cells were then baked at 80 °C with gentle compression for 2 hr.

680 To assemble a DNA-carpet in a flow cell, small unilamellar vesicles (SUVs) of 1,2-dioleoyl-*sn*-
681 glycero-3-phosphocholine (DOPC) and 1,2-dioleoyl-*sn*-glycero-3-phosphoethanolamine-N-
682 (biotinyl) (DOPE-Biotin) (Avanti Polar Lipids) were prepared as follows. 0.5 ml of DOPC (25
683 mg/ml chloroform) was mixed with 5 µl of DOPE-biotin (25 mg/ml chloroform) in a glass test
684 tube and most of the solvent removed *via* evaporation under a nitrogen flow. The remaining solvent
685 was removed by drying in a SpeedVac (Savant) at 42 °C for 1 hr followed by a further 1 hr at room
686 temperature. 2.5 ml of degassed TK150 buffer (25 mM Tris.HCl pH 7.5, 150 mM KCl) was then
687 added and the lipids stored, covered under nitrogen gas overnight. The lipids were then
688 resuspended by vortexing and sonicated (70-80 watts, 30 sec on, 10 sec off) in a cup horn with
689 water chiller set to 16 °C (QSonica) until transparent. The resulting solution of SUVs was then
690 filtered through a 0.22 µm filter, aliquoted and stored under nitrogen gas at 4 °C for up to 4 weeks.

691 To prepare biotinylated salmon sperm DNA for DNA-carpets 10 mg/ml salmon sperm DNA
692 (Thermo Fisher) was sonicated for 5 min (110 watts, 10 sec on, 10 sec off) to produce short
693 fragments. Sonicated salmon sperm DNA was then diluted to 1 mg/ml in Terminal Transferase
694 buffer (NEB) with 0.25 mM $CoCl_2$, 40 µM Biotin-14-dCTP (Thermo Fisher) and 1 unit/µl

695 Terminal Transferase (NEB). The DNA was incubated at 37 °C for 30 min, then the reaction
696 stopped by heat inactivation at 75 °C for 20 min. Free Biotin-14-dCTP was removed by extensive
697 buffer exchange with TE buffer (10 mM Tris.HCl pH 8, 0.1 mM EDTA) in a 100 kDa Amicon
698 Ultra spin concentrator (Millipore). The biotinylated DNA was then concentrated to ~10 mg/ml
699 and stored at -20 °C until needed.

700 To assemble a DNA-carpet, the DOPC—DOPE-biotin SUV solution was diluted to 1 mg/ml in
701 500 μl degassed TN150MC buffer (25 mM Tris.HCl pH7.5, 150 mM NaCl, 5 mM $MgCl_2$, 0.1 mM
702 $CaCl_2$) and warmed to 37 °C. Approximately 300 μl of SUV solution was then infused into a pre-
703 warmed flow cell and incubated at 37 °C for 1 hr. Excess SUVs were washed out with 500 μl
704 warmed, degassed TN150MC buffer at 100 μl/min. 300 μl of a solution of 1 mg/ml neutravidin
705 (Thermo Fisher) in warmed, degassed TN150MC buffer was then infused at a rate of 100 μl/min
706 into the flow cell and incubated at 37 °C for 30 min. Excess neutravidin was washed out with
707 TN150MC buffer as above, and the flow cell infused with 100 μl of a solution containing 1 mg/ml
708 biotinylated sonicated salmon sperm DNA (as prepared above) in warmed, degassed TN150MC
709 buffer and incubated at 37 °C for 30 min. The ports of the flow cell were sealed with parafilm and
710 stored at 4 °C for up to a week.

711 Prior to use, excess DNA was removed by infusion of 300 μl 0.22 μm filtered and degassed TIRFM
712 buffer (50 mM HEPES.KOH pH 7.5, 300 mM K-glutamate, 50 mM NaCl, 10 mM $MgCl_2$, 0.1 mM
713 $CaCl_2$, 2 mM DTT, 0.1 mg/ml α-casein, 0.6 mg/ml ascorbic acid, 10% glycerol) with addition of
714 1 mg/ml α-casein and 1 mM ATPγS and the flow cell incubated at room temperature for 30 min.

715 Conversion of the fluorescence signal detected in TIRF microscopy to the DNA-carpet-bound
716 protein densities was done following the procedure described in the legend of Figure S4 in
717 (Vecchiarelli et al., 2016).

718 *Fluorescence Recovery After Photobleaching (FRAP).*

719 For FRAP experiments, 488 nm solid-state and 630 nm diode laser was focused to the back focal
720 plane of the objective through an appropriate dichroic mirror (Di01-R405/488/561/635-25x36,
721 Semrock) through the objective lens to illuminate a ~5 or ~10 μm (for 488 nm or 630 nm,
722 respectively) diameter spot in the center of the sample area. The laser power was adjusted for
723 ~80 % bleaching with 5 s exposure for the eGFP or Alexa 647 signals, and four cycles of
724 bleaching/recovery were recorded for each sample and averaged.

725 *Magnetic Tweezers-based DNA condensation assay.*

726 The magnetic tweezer setup and assays conducted with it were performed as previously described
727 (Seol and Neuman, 2011; Seol et al., 2016).

728 The ability of $ParB_F$ to condense *parS*$_F$-containing DNA (spDNA) was tested by a custom-built
729 magnetic tweezer setup. In brief, two permanent magnets were used to apply force to micron sized
730 magnetic beads individually tethered to the coverslip of a one inlet flow cell by 5 kb pET28a
731 plasmid-derived DNA tethers. The distance the magnets were held from the beads, and hence the
732 force exerted upon them, was controlled by a linear motor that vertically positions the magnets.

733 5kb DNA substrates were generated by PCR using either pET28a-*parS*$_F$ plasmid (for *parS*$_F$-
734 containing DNA) or pET28a as templates. pET28-*parS*$_F$ DNA plasmid was generated by cloning
735 570 bp DNA segment containing 12 repeats of *parS*$_F$ native sequence from F-plasmid into pET28a
736 between the BamHI and SphI restriction sites.

737 Primers used for the PCR contained an extra non-complementary 15 nt at their 5' ends to encode
738 BsaI restriction sites. The PCR reaction yields a 5.2 kb product incorporating two BsaI restriction
739 sites at its termini. Digestion of this product was followed by ligation with 500 bp DNA "handles"
740 containing either multiple biotin or digitoxin labels. These handles were also generated by Taq-
741 based PCR using pBlueScript II KS as the template, pBlueScript II KS forward (5'- GCT GGG
742 TCT CGG TTG TTC CCT TTA GTG AGG GTT AAT TG) and pBlueScript II KS reverse (5'-
743 GCT GGG TCT CGT GGT TTC CCT TTA GTG AGG GTT AAT TG) primers and either 60 μM
744 biotin-16-dUTP or digoxigenin-11-dUTP (Roche). This results in a 5 kb DNA tether which can be
745 attached to a streptavidin coated magnetic bead at one end and an anti-digoxigenin coverslip
746 surface at the other.

747 ParB$_F$ samples were prepared in modified ATPase buffer (50 mM HEPES.KOH pH 7.5, 100 mM
748 KCl, 5 mM $MgCl_2$, 2 mM DTT, 10 mg/ml BSA and 0.1% Tween-20) and infused into a flow cell
749 containing tethered magnetic beads held at 5 pN of force. After the chamber was filled, the flow
750 was stopped, and the force reduced to 0.05 pN. The height of beads was tracked by analysis of
751 diffraction rings generated by illumination of the beads from above and observed with an objective
752 positioned below the flow cell. The extent of condensation by ParB was monitored by the decrease
753 in the height of the beads at 0.05 and 5 pN as compared to controls without protein.

Acknowledgements

We are grateful to helpful suggestions and discussion of our colleagues Barbara Funnell, David Lane, Michiyo Mizuuchi, Andrea Volante, Min Li, Masaki Osawa, William Carlquist and Shannon Mckie, to Esme Neuman for help in preparation of figures 1 and 7, and to Min Li for help in preparation of Figures 2—figure supplement 3. We thank Stephan Gruber and his colleagues for sharing their findings with us prior to publication. This work was supported by the intramural research fund for National Institute of Diabetes and Digestive and Kidney Diseases (K.M.); the National Heart, Lung, and Blood Institute (K.C.N.), National Institutes of Health, Department of Human Services.

764 **References**

765 Ah-Seng, Y., Lopez, F., Pasta, F., Lane, D., and Bouet, J.Y. (2009). Dual role of DNA in regulating
766 ATP hydrolysis by the SopA partition protein. J Biol Chem *284*, 30067-30075.

767 Ah-Seng, Y., Rech, J., Lane, D., and Bouet, J.Y. (2013). Defining the role of ATP hydrolysis in
768 mitotic segregation of bacterial plasmids. PLoS Genet *9*, e1003956.

769 Baxter, J.C., and Funnell, B.E. (2014). Plasmid Partition Mechanisms. Microbiol Spectr *2*.

770 Bouet, J.Y., Surtees, J.A., and Funnell, B.E. (2000). Stoichiometry of P1 plasmid partition
771 complexes. J Biol Chem *275*, 8213-8219.

772 Breier, A.M., and Grossman, A.D. (2007). Whole-genome analysis of the chromosome
773 partitioning and sporulation protein Spo0J (ParB) reveals spreading and origin-distal sites on the
774 Bacillus subtilis chromosome. Mol Microbiol *64*, 703-718.

775 Chen, B.-W., Lin, M.-H., Chu, C.-H., Hsu, C.-E., and Sun, Y.-J. (2015). Insights into ParB
776 spreading from the complerx structure of Spo0J and parS. Proc Natl Acad Sci U S A *112*, 6613-
777 6618.

778 Davey, M.J., and Funnell, B.E. (1994). The P1 plasmid partition protein ParA. A role for ATP in
779 site-specific DNA binding. J Biol Chem *269*, 29908-29913.

780 Davis, M.A., Martin, K.A., and Austin, S.J. (1992). Biochemical activities of the parA partition
781 protein of the P1 plasmid. Mol Microbiol *6*, 1141-1147.

782 Ebersbach, G., and Gerdes, K. (2004). Bacterial mitosis: partitioning protein ParA oscillates in
783 spiral-shaped structures and positions plasmids at mid-cell. Mol Microbiol *52*, 385-398.

784 Fung, E., Bouet, J.Y., and Funnell, B.E. (2001). Probing the ATP-binding site of P1 ParA: partition
785 and repression have different requirements for ATP binding and hydrolysis. EMBO J *20*, 4901-
786 4911.

787 Graham, T.G., Wang, X., Song, D., Etson, C.M., van Oijen, A.M., Rudner, D.Z., and Loparo, J.J.
788 (2014). ParB spreading requires DNA bridging. Genes & development *28,* 1228-1238.

789 Hatano, T., Yamaichi, Y., and Niki, H. (2007). Oscillating focus of SopA associated with
790 filamentous structure guides partitioning of F plasmid. Mol Microbiol *64*, 1198-1213.

791 Helsberg, M., and Eichenlaub, R. (1986). Twelve 43-base-pair repeats map in a cis-acting region
792 essential for partition of plasmid mini-F. J Bacteriol *165*, 1043-1045.

793 Hu, L., Vecchiarelli, A.G., Mizuuchi, K., Neuman, K.C., and Liu, J. (2017). Brownian Ratchet
794 Mechanism for Faithful Segregation of Low-Copy-Number Plasmids. Biophys J *112*, 1489-1502.

795 Ivanov, V., and Mizuuchi, K. (2010). Multiple modes of interconverting dynamic pattern
796 formation by bacterial cell division proteins. Proc Natl Acad Sci U S A *107*, 8071-8078.

797 Jalal, A.S., Tran, N.T., and Le, T.B. (2020). ParB spreading on DNA requires cytidine triphosphate
798 in vitro. eLife *9,* e 53515.

799 Le Gall, A., Cattoni, D.I., Guilhas, B., Mathieu-Demaziere, C., Oudjedi, L., Fiche, J.B., Rech, J.,
800 Abrahamsson, S., Murray, H., Bouet, J.Y., and Nollmann, M. (2016). Bacterial partition
801 complexes segregate within the volume of the nucleoid. Nat Commun *7*, 12107.

802 Leonard, T.A., Butler, P.J., and Lowe, J. (2005). Bacterial chromosome segregation: structure and
803 DNA binding of the Soj dimer--a conserved biological switch. EMBO J *24*, 270-282.

804 Lim, H.C., Surovtsev, I.V., Beltran, B.G., Huang, F., Bewersdorf, J., and Jacobs-Wagner, C.
805 (2014). Evidence for a DNA-relay mechanism in ParABS-mediated chromosome segregation.
806 eLife *3*, e02758.

807 Lutkenhaus, J. (2012). The ParA/MinD family puts things in their place. Trends Microbiol *20*,
808 411-418.

809 McLeod, B.N., Allison-Gamble, G.E., Barge, M.T., Tonthat, N.K., Schumacher, M.A., Hayes, F.,
810 and Barilla, D. (2017). A three-dimensional ParF meshwork assembles through the nucleoid to
811 mediate plasmid segregation. Nucleic acids research *45*, 3158-3171.

812 Modrich, M., and Zabel, D. (1976). Eco RI endonuclease Physical and catalytic properties of the
813 homogeneous enzyme. J Biol Chem *251*, 5866-5874.

814 Mori, H., Mori, Y., Ichinose, C., Niki, H., Ogura, T., Kato, A., and Hiraga, S. (1989). Purification
815 and characterization of SopA and SopB proteins essential for F plasmid partitioning. J Biol Chem
816 *264*, 15535-15541.

817 Motallebi-Veshareh, M., Rouch, D.A., and Thomas, C.M. (1990). A family of ATPases involved
818 in active partitioning of diverse bacterial plasmids. Mol Microbiol *4*, 1455-1463.

819 Murray, H., Ferreira, H., and Errington, J. (2006). The bacterial chromosome segregation protein
820 Spo0J spreads along DNA from parS nucleation sites. Mol Microbiol *61*, 1352-1361.

821 Osorio-Valeriano, M., Altegoer, F., Steinchen, W., Urban, S., Liu, Y., and Bange, G. (2019). ParB-
822 type DNA segregation proteins are CTP-dependent molecular switches. Cell 179, 1512-1524.

823 Pillet, F., Sanchez, A., Lane, D., Anton Leberre, V., and Bouet, J.Y. (2011). Centromere binding
824 specificity in assembly of the F plasmid partition complex. Nucleic acids research *39*, 7477-7486.

825 Ravin, N.V., Kuprianov, V.V., Gilcrease, E.B., and Casjens, S.R. (2003). Bidirectional replication
826 from an internal ori site of the linear N15 plasmid prophage. Nucleic acids research *31*, 6552-6560.

827 Ringgaard, S., van Zon, J., Howard, M., and Gerdes, K. (2009). Movement and equipositioning of
828 plasmids by ParA filament disassembly. Proc Natl Acad Sci U S A *106*, 19369-19374.

829 Rodionov, O., Lobocka, M., and Yarmolinsky, M. (1999). Silencing of genes flanking the P1
830 plasmid centromere. Science *283*, 546-549.

831 Sanchez, A., Cattoni, D.I., Walter, J.C., Rech, J., Parmeggiani, A., Nollmann, M., and Bouet, J.Y.
832 (2015). Stochastic Self-Assembly of ParB Proteins Builds the Bacterial DNA Segregation
833 Apparatus. Cell Syst *1*, 163-173.

834 Scholefield, G., Whiting, R., Errington, J., and Murray, H. (2011). Spo0J regulates the oligomeric
835 state of Soj to trigger its switch from an activator to an inhibitor of DNA replication initiation. Mol
836 Microbiol *79*, 1089-1100.

837 Schumacher, M.A., and Funnell, B.E. (2005). Structures of ParB bound to DNA reveal mechanism
838 of partition complex formation. Nature *438*, 516-519.

839 Schumacher, M.A., Piro, K.M., and Xu, W. (2010). Insight into F plasmid DNA segregation
840 revealed by structures of SopB and SopB-DNA complexes. Nucleic acids research *38*, 4514-4526.

841 Seol, Y., and Neuman, K.C. (2011). Magnetic tweezers for single-molecule manipulation.
842 Methods Mol Biol *783*, 265-293.

843 Seol, Y., Strub, M.P., and Neuman, K.C. (2016). Single molecule measurements of DNA helicase
844 activity with magnetic tweezers and t-test based step-finding analysis. Methods *105*, 119-127.

845 Soh, Y.M., Davidson, I.F., Zamuner, S., Basquin, J., Bock, F.P., Taschner, M., Veening, J.W., De
846 Los Rios, P., Peters, J.M., and Gruber, S. (2019). Self-organization of parS centromeres by the
847 ParB CTP hydrolase. Science *366*, 1129-1133.

848 Song, D., Rodrigues, K., Graham, T.G.W., and Loparo, J.J. (2017). A network of cis and trans
849 interactions is required for ParB spreading. Nucleic Acids Res *45*, 7106-7117.

850 Sugawara, T., and Kaneko, K. (2011). Chemophoresis as a driving force for intracellular
851 organization: Theory and application to plasmid partitioning. Biophysics (Nagoya-shi) *7*, 77-88.

852 Taylor, J.A., Pastrana, C.L., Butterer, A., Pernstich, C., Gwynn, E.J., Sobott, F., Moreno-Herrero,
853 F., and Dillingham, M.S. (2015). Specific and non-specific interactions of ParB with DNA:
854 implications for chromosome segregation. Nucleic acids research *43*, 719-731.

855 Vecchiarelli, A.G., Han, Y.W., Tan, X., Mizuuchi, M., Ghirlando, R., Biertumpfel, C., Funnell,
856 B.E., and Mizuuchi, K. (2010). ATP control of dynamic P1 ParA-DNA interactions: a key role for
857 the nucleoid in plasmid partition. Mol Microbiol *78*, 78-91.

858 Vecchiarelli, A.G., Hwang, L.C., and Mizuuchi, K. (2013). Cell-free study of F plasmid partition
859 provides evidence for cargo transport by a diffusion-ratchet mechanism. Proc Natl Acad Sci U S
860 A *110*, E1390-1397.

861 Vecchiarelli, A.G., Li, M., Mizuuchi, M., Hwang, L.C., Seol, Y., Neuman, K.C., and Mizuuchi,
862 K. (2016). Membrane-bound MinDE complex acts as a toggle switch that drives Min oscillation
863 coupled to cytoplasmic depletion of MinD. Proc Natl Acad Sci U S A *113*, E1479-1488.

864 Vecchiarelli, A.G., Mizuuchi, K., and Funnell, B.E. (2012). Surfing biological surfaces: exploiting
865 the nucleoid for partition and transport in bacteria. Mol Microbiol *86*, 513-523.

866 Vecchiarelli, A.G., Neuman, K.C., and Mizuuchi, K. (2014). A propagating ATPase gradient
867 drives transport of surface-confined cellular cargo. Proc Natl Acad Sci U S A *111,* 4880-4885.

868 Watanabe, E., Wachi, M., Yamasaki, M., and Nagai, K. (1992). ATPase activity of SopA, a protein
869 essential for active partitioning of F plasmid. Molecular & general genetics : MGG *234*, 346-352.

870 Yamaichi, Y., and Niki, H. (2000). Active segregation by the Bacillus subtilis partitioning system
871 in Escherichia coli. Proc Natl Acad Sci U S A *97*, 14656-14661.

872

873 **Figure and Table legends**

874 **Figure 1.** *Schematic of flow cell setup for visualizing the binding and dissociation of*
875 *fluorescent proteins on DNA-carpet*.

876 $ParA_F$-eGFP and $ParB_F$-Alexa647 proteins were flowed over a dense carpet of nsDNA attached to
877 the supported lipid bilayer coated surface of a flow cell. TIRF microscopy permits selective
878 detection of the DNA-carpet bound proteins. Sample solution and wash buffer, as specified for

879 each experiment, were infused *via* two syringes at different infusion rates from separate inlets into
880 a Y-shaped flow cell. A laminar boundary separates the two solutions downstream of the flow
881 convergence point at the Y-junction. At the midpoint across the flow channel, downstream but
882 close to the flow convergence point where the observations are made, the DNA-carpet area is
883 exposed to the syringe content of the higher infusion rate. When the infusion rates of the two
884 syringes are switched, the laminar boundary moves across the observation area and the solution
885 flowing over the area switches. By switching the infusion rates of the two syringes repeatedly,
886 multiple DNA-carpet-bound protein complex assembly and wash cycles can be recorded.

887 **Figure 2.** *Monomeric $ParB_F^{1-42}$-mCherry can activate $ParA_F$ for nsDNA binding in the*
888 *presence of ATPγS by forming a ~1:1 complex.*

889 Protein sample solution in the presence of ATPγS (1 mM) was infused into nsDNA-carpeted flow
890 cell at a constant flow to monitor the protein binding to the nsDNA, and the sample solution was
891 switched to a wash buffer containing ATPγS to monitor protein dissociation from nsDNA. (A and
892 B) Binding to, and dissociation from, nsDNA of $ParA_F$-eGFP (1 μM) or $ParB_F$-Alexa647 (2 μM)
893 were measured separately. (C) $ParB_F^{1-42}$-mCherry (10 μM) and $ParA_F$-eGFP (1 μM) preincubated
894 with ATPγS were infused into the nsDNA-carpeted flow cell and (D) washed with buffer
895 containing ATPγS. (E) The washing experiment of D was repeated with wash buffer containing
896 ATPγS and $ParB_F^{1-42}$-mCherry (10 μM). For the parameters of the time courses of above
897 experiments and subsequent experiments of the same type in this study, see Table 1. The
898 $ParB_F$:$ParA_F$ ratio was calculated from carpet-bound densities of the two proteins measured in
899 parallel, and summarized in Table 1. (F) $ParA_F$-ATPase activity (expressed as turnover rate per

900 $ParA_F$ monomer) was measured in the presence of EcoRI-digested pBR322 DNA (60 μg/ml) and
901 different concentrations of $ParB_F^{1-42}$. Inset shows a plot with expanded abscissa. (G) $ParA_F$-ATPase
902 activity was measured as above in the presence of dimeric $ParB_F^{1-42}$-mCherry-$EcoRI^{E111Q}$. The
903 parameters of ATPase stimulation curves in these and subsequent figures are summarized in Table
904 2.

905 **Source Data 1:** Numerical data for figure 2 panels A-E (Microsoft Excel).

906 **Source Data 2:** Numerical data for figure 2 panels F, G (Microsoft Excel).

907 **Figure supplement 1:** *G*el filtration column elution profile of $ParB_F^{1-42}$-mCherry.

908 **Figure supplement 2—Source data 1:** FRAP of $ParA_F$-eGFP and $ParB_F^{1-42}$-mCherry on DNA-
909 carpet.

910 **Figure supplement 3:** Comparison of possible structural domain arrangements of artificially
911 dimeric $ParB_F^{1-42}$-mCherry-$EcoRI^{E111Q}$ to $ParB_F$ structures in the absence or presence of C-
912 nucleotide.

913 **Figure supplement 4—Source data 1:** $ParA_F$ ATPase stimulation by $ParB_F^{1-42}$-mCherry-
914 $EcoRI^{E111Q}$ is not influenced by the addition of DNA fragment containing EcoRI recognition
915 sequence.

916 **Figure 3.** *$ParB_F^{1-42\ R36A}$-mCherry dissociates faster from nsDNA-carpet-bound $ParA_F$-ATPγS*
917 *dimer, and $ParA_F$-ATPase activation requires higher $ParB_F^{1-42\ R36A}$ concentration.*

918 (A) $ParB_F^{1-42\ R36A}$-mCherry (10 μM) and $ParA_F$-eGFP (1 μM) preincubated with ATPγS were
919 infused into the nsDNA-carpeted flow cell and then (B) washed with buffer containing ATPγS.
920 (C) The washing experiment of B was repeated with buffer containing ATPγS and $ParB_F^{1-42\ R36A}$-
921 mCherry (10 μM). (D) $ParA_F$-ATPase activity was measured in the presence of EcoRI-digested
922 pBR322 DNA (60 μg/ml) as a function of $ParB_F^{1-42\ R36A}$ concentration. See Figure 2 legend and
923 Tables 1 and 2 for additional details.

924 **Source data 1:** Numerical data for figure 3 panels A-C (Microsoft Excel).

925 **Source data 2:** Numerical data for figure 3 panels D (Microsoft Excel).

926 **Figure 4.** *$parS_F$ DNA alters protein stoichiometry of the $ParA_F$—$ParB_F$ complex formed prior*
927 *to ATP hydrolysis and the extent of $ParA_F$-ATPase activation by $ParB_F$.*

928 (A) $ParA_F$-eGFP (1 μM) and $ParB_F$-Alexa647 (2 μM) preincubated with ATPγS were infused into
929 the nsDNA-carpeted flow cell and then (B) washed with buffer containing ATPγS. (C and D) As
930 A and B except the sample included 24bp *$parS_F$* DNA fragment (1.1 μM). (E) $ParA_F$-ATPase
931 activity was measured in the presence of EcoRI-digested pBR322 DNA (60 μg/ml), different
932 concentrations of $ParB_F$ and either a *$parS_F$*-DNA fragment or a DNA fragment with a scrambled
933 sequence (1.1-fold higher concentrations than the $ParB_F$ dimers). See Figure 2 legend and Tables
934 1 and 2 for additional details.

935 **Source data 1:** Numerical data for figure 4 panels A-D (Microsoft Excel).

936 **Source data 2:** Numerical data for figure 4 panels E (Microsoft Excel).

937 **Figure supplement 1—Source data 1:** Numerical data for Figure 4—figure supplement 1

938 (Microsoft Excel).

939 **Figure supplement 2—Source data 1:** Numerical data for Figure 4—figure supplement 2

940 (Microsoft Excel).

941 **Figure 5.** *CTP and $parS_F$ together alter interactions between $ParB_F$ and $ParA_F$ dimers.*

942 (A) $ParA_F$-eGFP (1 μM) and $ParB_F$-Alexa647 (2 μM) preincubated with ATPγS and CTP (2mM)

943 were infused into the nsDNA-carpeted flow cell and then washed with buffer containing ATPγS

944 and CTP. (B) As in A, except a 24 bp $parS_F$ fragment (1.1 μM) was added to the sample mixture.

945 (C) As in B, except CTP was replaced by CDP. For binding curves, see Figure 5—figure

946 supplement 1A-C. (D) $ParA_F$ (1 μM), $ParB_F$-Alexa647 (2 μM) and Alexa488-labeled 24 bp $parS_F$

947 fragment (1.1 μM) preincubated with ATPγS or ATPγS plus CTP (2mM) were infused into the

948 nsDNA-carpeted flow cell and after 240 sec, the ratio of the carpet-bound $parS_F$ fragment and

949 $ParB_F$ dimer was measured. (E) $ParA_F$-ATPase activity was measured in the presence of EcoRI-

950 digested pBR322 DNA (60 μg/ml), different concentrations of $ParB_F$ and either no C-nucleotide,

951 or 2mM CTP. Inset shows data in the presence of CTP with expanded abscissa. (F) As in E except

952 the reactions also contained 24 bp $parS_F$ fragment (1.1-fold higher concentrations than $ParB_F$

953 dimers). Inset shows data in the presence of $parS_F$ and CTP with expanded abscissa. See Figure 2

954 legend and Tables 1 and 2 for additional details.

955 **Source data 1:** Numerical data for figure 5 panels A-D (Microsoft Excel).

956 **Source data 2:** Numerical data for figure 5 panels E, F (Microsoft Excel).

957 **Figure supplement 1—Source data 1:** Numerical data for Figure 5—figure supplement 1

958 (Microsoft Excel).

959 **Figure supplement 2—Source data 1:** Numerical data for Figure 5—figure supplement 2
960 (Microsoft Excel).

961 **Figure 6.** *Magnetic tweezers measurements of $parS_F$ and CTP-dependent DNA*
962 *condensation by $ParB_F$.*

963 (A) Schematic showing the magnetic tweezers DNA condensation assay. One end of a 5 kb DNA
964 molecule is attached to the surface of a flow-cell and the free end is attached to a 1 μm magnetic
965 bead (brown sphere). The DNA extension (Ex) was measured by tracking the bead height above
966 the cover glass surface at two different forces; 0.05 pN (low force, lf), and 5 pN (high force, hf).
967 The extent of DNA condensation was estimated from the difference in DNA extension with and
968 without $ParB_F$. (B) Changes in extension at low force ($dEx^{lf} = Ex^{lf} - Ex_0^{lf}$), left panel, and at high
969 force ($dEx^{hf} = Ex^{hf} - Ex_0^{hf}$), right panel, for 7 different conditions plotted as a function of $ParB_F$
970 concentration. The extension values were the averages of the last 5 seconds of the extension at low
971 force (circles) and the first 5 seconds of the extension at high force (triangles). Error bars represent
972 standard error of means (SEM). Different conditions are color coded as follows. Purple: $parS_F$-
973 DNA tether with WT $ParB_F$ and CTP; light blue: $parS_F$-DNA tether with WT $ParB_F$ and CDP; dark
974 blue: nsDNA tether with WT $ParB_F$ and CTP; red: $parS_F$-DNA tether with $ParB_F^{R121A}$ and CTP;
975 orange: nsDNA tether with $ParB_F^{R121A}$ and CTP. For comparison with condensation in the presence
976 of CTP, dEx data of $parS_F$-DNA tether (purple) and nsDNA tether (blue) with WT $ParB_F$ without
977 CTP are displayed (inset, open circles for 0.05 pN, triangle for 5 pN respectively). (C) The
978 condensation probabilities at 0.1 μM $ParB_F$ for 5 different conditions at 0.05 pN and 5 pN. The
979 condensation probability was calculated by dividing the number of DNA tethers that exhibited

980 DNA condensation by the total number of DNA tethers for each measurement condition. Except
981 for *parS*$_F$-DNA with WT ParB$_F$ and CTP, all conditions show either minimal or negligible
982 condensation probabilities. The different conditions are color-coded as indicated in B and the
983 diagonal stripes indicates probabilities at 5 pN. Error bars represent standard error of means (SEM).
984 **Source data 1:** Numerical data for figure 6 panel A (Microsoft Excel).
985 **Source data 2:** Numerical data for figure 6 panel B-left (Microsoft Excel).
986 **Source data 3:** Numerical data for figure 6 panel B-right (Microsoft Excel).
987 **Source data 4:** Numerical data for figure 6 panel C (Microsoft Excel).
988 **Figure supplement 1—Source data 1:** Numerical data for Figure 6—figure supplement 1A
989 (Microsoft Excel).
990 **Figure supplement 1—Source data 2:** Numerical data for Figure 6—figure supplement 1B
991 (Microsoft Excel).
992 **Figure supplement 2—Source data 1:** Numerical data for Figure 6—figure supplement 2
993 (Microsoft Excel).
994 **Figure supplement 3—Source data 1:** Numerical data for Figure 6—figure supplement 3
995 (Microsoft Excel).

996 **Figure 7.** *Cartoon of the proposed pre-ATPase-activation complexes of ParA*$_F$ *and ParB*$_F$.

997 (A) Pictograms of nsDNA, *parS*$_F$-DNA, ParA$_F$ monomer/dimer and ParB$_F$ domains with binding
998 ligand designations. The CTPase domains of a ParB$_F$ dimer fold forming a single globular domain
999 on binding CTP, bringing the two ParA$_F$-binding domains into close proximity. (B) ParA$_F$-binding
1000 domain, ParB$_F^{1-42}$ alone can convert ParA$_F$ monomers to DNA-binding-competent dimers in the

1001 presence of ATPγS by forming an $A_2B^{1-42}{}_2$ complex (top). $ParB_F$ dimers in the absence of CTP
1002 convert $ParA_F$ monomers to DNA-binding-competent dimers in the presence of ATPγS by
1003 straddling a $ParA_F$ dimer to form an A_2B_2 complex (middle). In the presence of CTP, the close
1004 proximity of the $ParA_F$-binding domains of the $ParB_F$ dimer prevents A_2B_2 complex formation and
1005 instead an A_2B_4 complex assembles on nsDNA in the presence of ATPγS (bottom). (C) In the
1006 presence of $parS_F$ and CTP, $ParB_F$ dimers load on to the $parS_F$-DNA and spread to adjacent DNA
1007 regions while adopting a state that enables faster assembly of A_2B_4 complexes. Considering the
1008 requirements for efficient partition complex motion by diffusion-ratchet mechanism based on the
1009 chemophoretic principle of force generation, we propose a significant energy barrier that slows the
1010 formation of the ATP hydrolysis-competent A_2B_4 complex. This energy barrier partially decouples
1011 $ParA_F$—$ParB_F$ association-dissociation dynamics from ATP hydrolysis, which triggers $ParA_F$
1012 dissociation from the nucleoid.

1013 **Table 1.** *Apparent disassembly or exchange rate constants (min^{-1}) and $ParB_F/ParA_F$ ratio*
1014 *from fits of TIRFM wash and FRAP experiments.*

1015 The apparent dissociation (or FRAP) rate constants (k_{off}) were obtained for individual time-
1016 trajectories by single-exponential curve fitting (except ** where the rate of the faster decay, (68
1017 +/- 0.5%) of a double-exponential fit is shown), and the mean and SEM for the set of independent
1018 experiments are shown in **bold** (except *where standard deviation among non-independent repeats
1019 within an experiment is shown). (N is the number of separate experiments, with total number of
1020 binding/wash cycles for repeated data collection in parenthesis.) ParA:ParB ratios were calculated
1021 from the final phase of the individual association time-trajectories (except *** where it was based

1022 on the beginning part of the washing phase in the presence of $ParB_F^{1-42\ R36A}$), and the mean and
1023 SEM for the set of independent experiments are shown in *italics*. N.D., not done.

1024 **Table 2.** *ATPase fit parameters.*

1025 ATPase measurements were performed with $ParA_F$ (1 μM) and different mutants of $ParB_F$, 60
1026 μg/ml EcoRI-digested pBR322 DNA plus Scram- or $parS_F$-DNA fragment and CTP or CDP, as
1027 indicated in the column headings. Assays were repeated "*N*" times, each data set of an assay was
1028 fit after subtraction of background measured without $ParA_F$ to a modified Hill equation: $v - v_0 =$
1029 $(v_{max}\ [B]^n) / (K_A^n + [B]^n)$, and the mean and standard error of the mean (SEM) of the fit parameters
1030 for the *N* measurements are shown. For [B] on the x-axis, total $ParB_F$ concentration was used
1031 instead of free $ParB_F$ concentration due to technical issues in estimating the free $ParB_F$
1032 concentration and the meanings of $\mathbf{K_A}$ and the cooperativity factor **n** here differ from those in the
1033 standard adaptation of the Hill equation. $\boldsymbol{v_{max}}$ is the maximum stimulated $ParA_F$ ATPase turnover
1034 rate, $\mathbf{K_A}$ is the apparent <u>total</u> concentration of $ParB_F$ necessary for half maximum stimulation, and
1035 **n** is the apparent cooperativity coefficient.

1036

1037 **Figure Supplement Legends:**

1038 **Figure 2—figure supplement 1.**

1039 *G*el filtration column elution profile of $ParB_F^{1-42}$-mCherry.

1040 The elution profile of $ParB_F^{1-42}$-mCherry on a Superose 6 3.2/300 column (GE Healthcare) with a
1041 standard curve generated using a protein standards kit (GE Healthcare). The molecular weight of
1042 $ParB_F^{1-42}$-mCherry was estimated to be ~35 kDa, close to the predicted molecular weight for a
1043 monomer of ~33 kDa.

1044 **Figure 2—figure supplement 2.**

1045 FRAP of $ParA_F$-eGFP and $ParB_F^{1-42}$-mCherry on DNA-carpet.

1046 $ParB_F^{1-42}$-mCherry exchanged significantly faster than $ParA_F$ after photo-bleaching. Data have been
1047 normalized to the maximum fluorescence recovery. The data were fitted to a single-exponential
1048 curve for $ParA_F$ and a double-exponential curve for $ParB_F$, which was not well fit with a single-
1049 exponential recovery curve. $ParA_F$ recovered with k_{excg} ~2.0 min^{-1}, and $ParB_F$ recovered with k_{excg}
1050 ~15 min^{-1} for the faster (68%), and ~2.0 min^{-1} for the slower, recovery components. Multi-
1051 exponential recovery kinetics can be explained by the relatively large bleached area causing
1052 variable diffusion distance for the unbleached molecules need to travel for full fluorescence
1053 recovery of the bleached area (this affects recovery of faster recovering components more
1054 significantly). An alternative explanation that assumes a 30% population of stable $ParA_F$-$ParB_F^{1-}$
1055 ^{42}-mCherry complex is unlikely since the buffer wash experiment (Figure 2D) did not support the
1056 presence of such a species.

1057 **Figure 2—figure supplement 3.**

1058 Comparison of possible structural domain arrangements of artificially dimeric $ParB_F^{1-42}$-mCherry-
1059 $EcoRI^{E111Q}$ (A), $ParB_F$ dimer structure in the absence (B) and presence (C) of C-nucleotide. This
1060 figure depicts montages of domain structures connected by gray lines representing presumed
1061 flexible linkers. The structures of the protein domains are based on the following PDB files: EcoR1
1062 (dark green): 1qc9, mCherry (pale yellow): 2h5q, ParB dimerization domain (gray): 1zx4, ParB
1063 DNA-binding domain (dark blue) plus CTPase domain (pale blue) in the absence of C-nucleotide:
1064 4umk, ParB DNA-binding domain plus CTPase domain bound to CDP: 6sdk. The dark red helix
1065 symbolizes the $ParA_F$ interaction domain, which is expected to form an α-helix upon binding $ParA_F$.
1066 The domain arrangement in B is loosely based on the proposal by Chen et al., (2015), which is
1067 based on the SAXS envelope of $ParB_{Hp}$ dimer in the absence of C-nucleotide.

1068 **Figure 2—figure supplement 4.**

1069 $ParA_F$ ATPase stimulation by $ParB_F^{1-42}$-mCherry-$EcoRI^{E111Q}$ is not influenced by the addition of
1070 DNA fragment containing EcoRI recognition sequence.

1071 (A) $ParA_F$-ATPase activation curve of $ParB_F^{1-42}$-mCherry-$EcoRI^{E111Q}$ in the absence of the EcoRI
1072 sequence duplex (Figure 2G) is shown for comparison. (B) $ParA_F$-ATPase activity was measured
1073 in the presence of EcoRI-digested pBR322 DNA (60 μg/ml), 77 bp duplex DNA fragment
1074 containing two EcoRI recognition sequences (5'-
1075 GAATTCCGAGTGGGACCGTGGTCCCAGTCTGATTATCAGACCGAGAATTCAAGTTGG

1076 GACCGTGGTCCCAAGAGAAT, plus complement; 1.5 μM) and different concentrations of

1077 dimeric $ParB_F^{1-42}$-mCherry-$EcoRI^{E111Q}$.

1078 **Figure 4—figure supplement 1.**

1079 Determination of $ParB_F$ monomer-dimer K_D by FRET.

1080 In order to estimate the K_D for dimerization of $ParB_F$ two batches of protein were separately labeled

1081 with Alexa 488 or Alexa 594 then mixed at equal concentrations, the sum of which are shown on

1082 the *x*-axis. The FRET efficiency was measured using a fluorescence plate reader (Clariostar Plus,

1083 BMG Labtech). Assuming the observed FRET efficiency linearly correlates to the fraction of the

1084 protein in the dimer state, the apparent K_D for dimerization of $ParB_F$ was estimated to be ~18.5 nM.

1085 **Figure 4—figure supplement 2.**

1086 Mutation of a BoxII residue R121A does not affect the affinity of $ParB_F^{R121A}$ for $parS_F$, but neither

1087 the protein stoichiometry of the $ParA_F$-$ParB_F^{R121A}$ complex assembled on nsDNA prior to ATP

1088 hydrolysis, nor the extent of $ParA_F$-ATPase activation by $ParB_F^{R121A}$ is impacted by the presence

1089 of $parS_F$.

1090 $ParA_F$ (1 μM) and $ParB_F^{R121A}$ (2 μM) were preincubated in the presence of ATPγS either without

1091 (A) or together with 24 bp $parS_F$ DNA fragment (1.1 μM, C), infused into to the DNA-carpeted

1092 flow cell and washed with buffer containing ATPγS (B, D). (E) $ParA_F$ ATPase activation by

1093 $ParB_F^{R121A}$ was measured in the presence of EcoRI-digested pBR322 DNA (60 μg/ml) and different

1094 concentrations of $ParB_F^{R121A}$ either in the absence (black line) or presence (red line) of $parS_F$ (at

1095 10% excess of the dimer concentrations of $ParB_F^{R121A}$). (F) The binding of $ParB_F$ or $ParB_F^{R121A}$ to
1096 0.1 nM P^{32}-labeled 24 bp *$parS_F$* DNA (left) or to 0.1 nM P^{32}-labeled 24 bp *scrambled* DNA (right)
1097 was measured by EMSA. A 4-12% gradient acrylamide gel was run in 1x TBE + 5 mM Mg_2Ac at
1098 4 °C for 1 hour, 150 V. The gels were quantified (bottom) to estimate the *parS* binding K_D of $ParB_F$
1099 and $ParB_F^{R121A}$.

1100 **Figure 5—figure supplement 1.**

1101 Binding curves for $ParA_F$ and $ParB_F$ with CDP or CTP associating with the DNA-carpet.
1102 (A) $ParA_F$-eGFP (1 μM) and $ParB_F$-Alexa647 (2 μM) preincubated in the presence of ATPγS and
1103 2 mM CTP were infused into the nsDNA-carpeted flow cell. (B) $ParA_F$-eGFP (1 μM) and $ParB_F$-
1104 Alexa647 (2 μM) preincubated in the presence of 24bp *$parS_F$* DNA fragment (1.1 μM), ATPγS
1105 and 2 mM CTP were infused into the nsDNA-carpeted flow cell. (C) $ParA_F$-eGFP (1 μM) and
1106 $ParB_F$-Alexa647 (2 μM) preincubated in the presence of 24bp *$parS_F$* DNA fragment (1.1 μM),
1107 ATPγS and 2 mM CDP were infused into the nsDNA-carpeted flow cell.

1108 **Figure 5—figure supplement 2.**

1109 Nucleotide specificity and CTPase activity of $ParB_F$ in the presence of different concentrations of
1110 CTP, in the presence or absence of *$parS_F$*.

1111 (A) NTPase activities of $ParB_F$ (0.84 μM) in the presence of 100 μM ribonucleoside triphosphates
1112 were measured in the CTPase buffer (Materials and Methods). (B) The CTP hydrolysis initial rate
1113 by $ParB_F$ (0.84 μM) was measured at different CTP concentrations to estimate the apparent CTP

1114 K_M with or without 100 nM $parS_F$ (24bp duplex with one copy of $ParB_F$ binding consensus
1115 sequence). (C) $parS_F$ concentration dependence of the CTPase activity of $ParB_F$ (0.84 μM, 100 μM
1116 CTP). Pronounced sigmoidal $parS_F$ concentration dependency of the CTPase stimulation was
1117 observed. This is in contrast to the hyperbolic $parS_{Bsu}$ concentration dependency reported for
1118 $ParB_{Bsu}$ (Soh et al., 2019). The mechanistic reason for this concentration dependency is currently
1119 under investigation. (D) CDP used in this study contained a compound that can be hydrolyzed by
1120 $ParB_F$ to release Pi. Time course of Pi production from 1 mM CDP in the presence of 0.84 μM
1121 $ParB_F$ is compared to reactions containing 5 to 150 μM CTP.

1122 **Figure 6—figure supplement 1.**

1123 Stepwise de-condensation of condensed DNA tethers in the presence of CDP or CTP by tensile
1124 force: condensation observed in the presence of CDP is unstable.

1125 (A) The extension of 6 DNA tethers containing $parS_F$ sequences (colored solid lines, left y-axis)
1126 were simultaneously measured at a force (green solid line, right y-axis) of 0.05 pN after the
1127 introduction of $ParB_F$ (0.1 μM) and CTP (1 mM). The tethers remained condensed for at least 85 s
1128 after the force was increased to 5 pN. Most increases in extension took place in discrete steps. (B)
1129 The same measurement as in (A) except that the DNA was condensed with 10-fold more $ParB_F$ (1
1130 μM) with CDP (1 mM). DNA condensation in the presence of CDP was quickly reversed under
1131 high force (5 pN). After the force was increased to 5 pN (time 0) the extension of all five DNA
1132 tethers increased to their full decondensed length (dashed line) within ~5 s.

1133 **Figure 6–figure supplement 2.**

1134 Tether condensation by $ParB_F$ is comparable for topologically constrained (supercoilable) and
1135 unconstrained (nicked) DNA.

1136 (A) The DNA tethers used for the condensation experiments were a mixture of torsionally
1137 constrained and unconstrained. Prior to condensation measurements, the magnetic beads attached
1138 to the end of the DNA molecules were rotated by rotating the external magnets in the magnetic
1139 tweezers instrument. Rotationally constrained DNA molecules are supercoiled by rotating the
1140 magnet, resulting in the formation of a plectoneme and a decrease in the extension of the DNA
1141 molecule. Torsionally unconstrained (typically nicked) DNA molecules are insensitive to the bead
1142 rotation and remain at the same extension (top). An example of this *in situ* discrimination between
1143 torsionally constrained and unconstrained DNA tethers is shown in the graph displaying the
1144 extension of 6 DNA molecules (bottom). The DNA extension decreased for 2 of the 6 DNA
1145 molecules after imposing -10 turns, indicating that these two molecules are rotationally constrained
1146 (left panel bottom). (B) Condensation, as measured by the change in extension reduction as a
1147 function of $ParB_F$ concentration is comparable for the topologically constrained (black squares)
1148 and unconstrained (grey squares) DNA molecules.

1149 **Figure 6—figure supplement 3.**

1150 DNA tethers without $parS_F$ sequence are not condensed by $ParB_F$ and $parS_F$ *in trans* in the
1151 presence of CTP.

1152 DNA tethers that did not contain a $parS_F$ site were not significantly condensed by the addition of
1153 $parS_F$ DNA fragment *in trans* with $ParB_F$ in the presence of CTP. The decreases in extension at

1154 0.05 pN (blue circle, left panel) and 5 pN (blue triangle, right panel) are plotted as a function of

1155 the concentration of ParB and $parS_F$, which were added together at stoichiometric concentrations.

1156

Source Data Files (one Excel file with 19 sheets)

Figure 2-Source Data 1:

Numerical data for Figure 2 panels A-E (Microsoft Excel).

Figure 2-Source Data 2:

Numerical data for Figure 2 panels F, G (Microsoft Excel).

Figure 2—figure supplement 2-Source Data 1:

Numerical data for Figure 2—figure supplement 2 (Microsoft Excel).

Figure 2—figure supplement 4-Source Data 1:

Numerical data for Figure 2—figure supplement 4 (Microsoft Excel).

Figure 3-Source Data 1:

Numerical data for Figure 3 panels A-C (Microsoft Excel).

Figure 3-Source Data 2:

Numerical data for Figure 3 panels D (Microsoft Excel).

Figure 4-Source Data 1:

Numerical data for Figure 4 panels A-D (Microsoft Excel).

Figure 4-Source Data 2:

Numerical data for Figure 4 panels E (Microsoft Excel).

Figure 4—figure supplement 1-Source Data 1:

Numerical data for Figure 4—figure supplement 1 (Microsoft Excel).

Figure 4—figure supplement 2-Source Data 1:

Numerical data for Figure 4—figure supplement 2 panels A-D and F (Microsoft Excel).

Figure 5-Source Data 1:

Numerical data for Figure 5 panels A-D (Microsoft Excel).

Figure 5-Source Data 2:

Numerical data for Figure 5 panels E, F (Microsoft Excel).

Figure 5—figure supplement 1-Source Data 1:

Numerical data for Figure 5—figure supplement 1 (Microsoft Excel).

Figure 5—figure supplement 2-Source Data 1:

Numerical data for Figure 5—figure supplement 2 (Microsoft Excel).

Figure 6-Source Data 1:

Numerical data for Figure 6 panel A (Microsoft Excel).

Figure 6-Source Data 2:

Numerical data for Figure 6 panel B-left (Microsoft Excel).

Figure 6-Source Data 3:

Numerical data for Figure 6 panels B-right (Microsoft Excel).

Figure 6-Source Data 4:

Numerical data for Figure 6 panels C (Microsoft Excel).

Figure 6—figure supplement 1-Source Data 1:

Numerical data for Figure 6—figure supplement 1A (Microsoft Excel).

Figure 6—figure supplement 1-Source Data 2:

Numerical data for Figure 6—figure supplement 1B (Microsoft Excel).

Figure 6—figure supplement 2-Source Data 1:

Numerical data for Figure 6—figure supplement 2 (Microsoft Excel).

Figure 6—figure supplement 3-Source Data 1:

1201 Numerical data for Figure 6—figure supplement 3 (Microsoft Excel).

1202

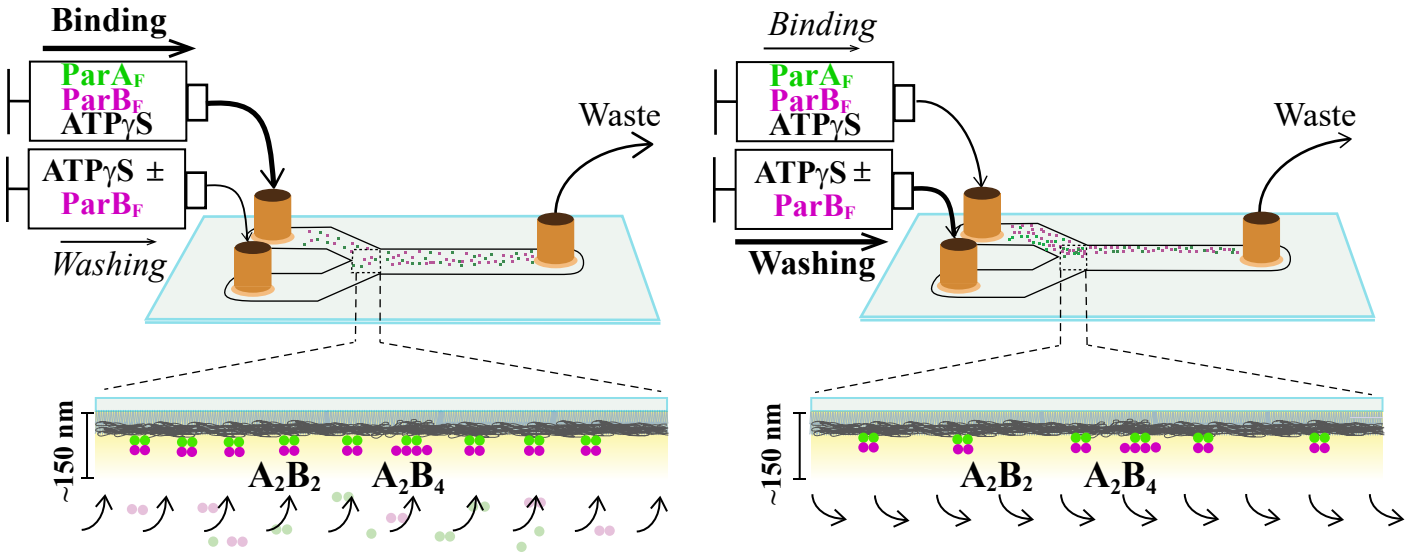
Binding
ParAF
ParBF
ATPγS
ATPγS ±
ParBF
Washing
Waste
~150 nm
A2B2
A2B4
Binding
ParAF
ParBF
ATPγS
ATPγS ±
ParBF
Washing
Waste
~150 nm
A2B2
A2B4

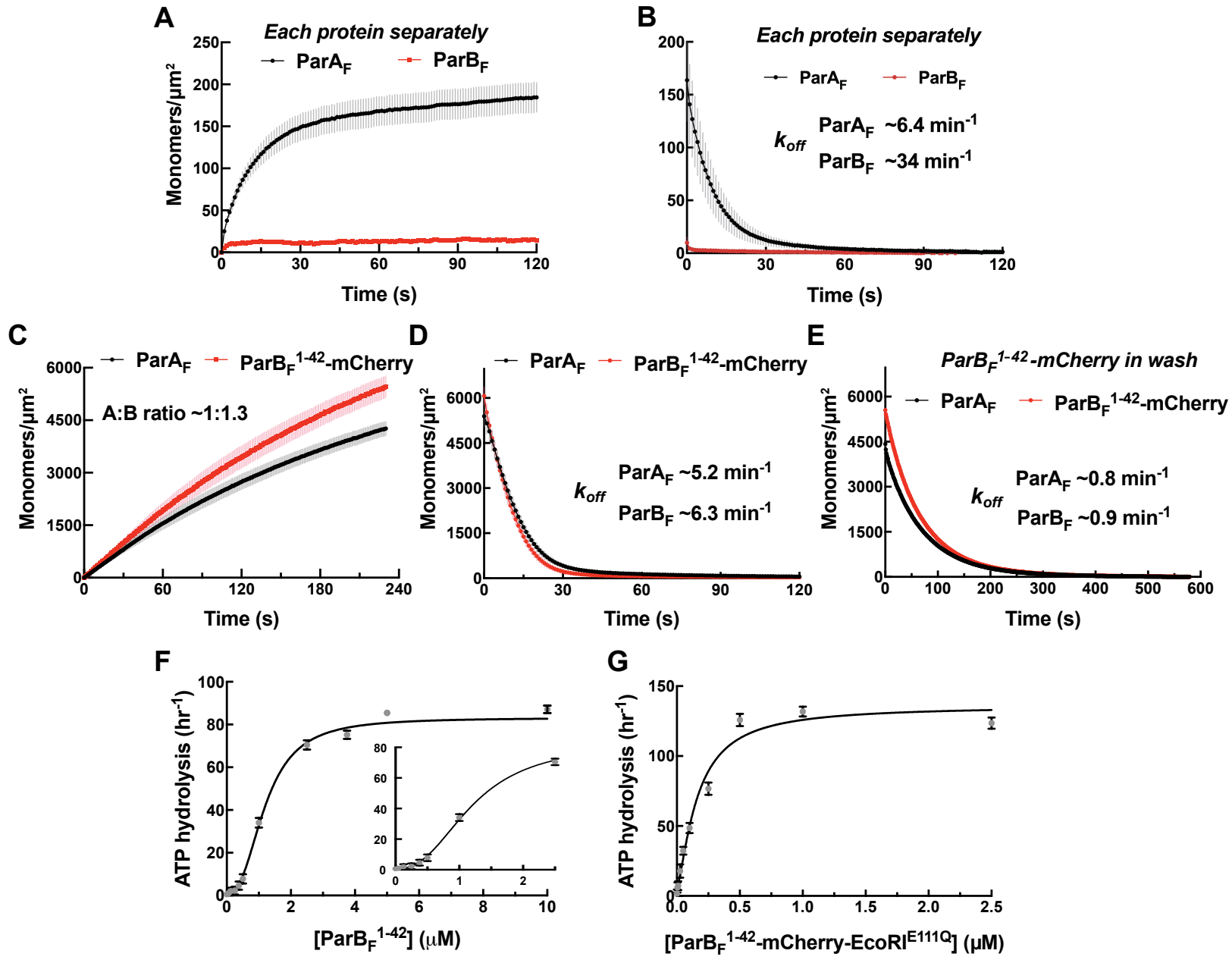
A
Each protein separately
ParA$_F$
ParB$_F$
Monomers/μm^2
Time (s)
B
Each protein separately
ParA$_F$
ParB$_F$
k_{off}
ParA$_F$ ~6.4 min^{-1}
ParB$_F$ ~34 min^{-1}
Time (s)
C
ParA$_F$
ParB$_F^{1-42}$-mCherry
A:B ratio ~1:1.3
Monomers/μm^2
Time (s)
D
ParA$_F$
ParB$_F^{1-42}$-mCherry
k_{off}
ParA$_F$ ~5.2 min^{-1}
ParB$_F$ ~6.3 min^{-1}
Monomers/μm^2
Time (s)
E
ParB$_F^{1-42}$-mCherry in wash
ParA$_F$
ParB$_F^{1-42}$-mCherry
k_{off}
ParA$_F$ ~0.8 min^{-1}
ParB$_F$ ~0.9 min^{-1}
Monomers/μm^2
Time (s)
F
ATP hydrolysis (hr^{-1})
[ParB$_F^{1-42}$] (μM)
G
ATP hydrolysis (hr^{-1})
[ParB$_F^{1-42}$-mCherry-EcoRI^{E111Q}] (μM)

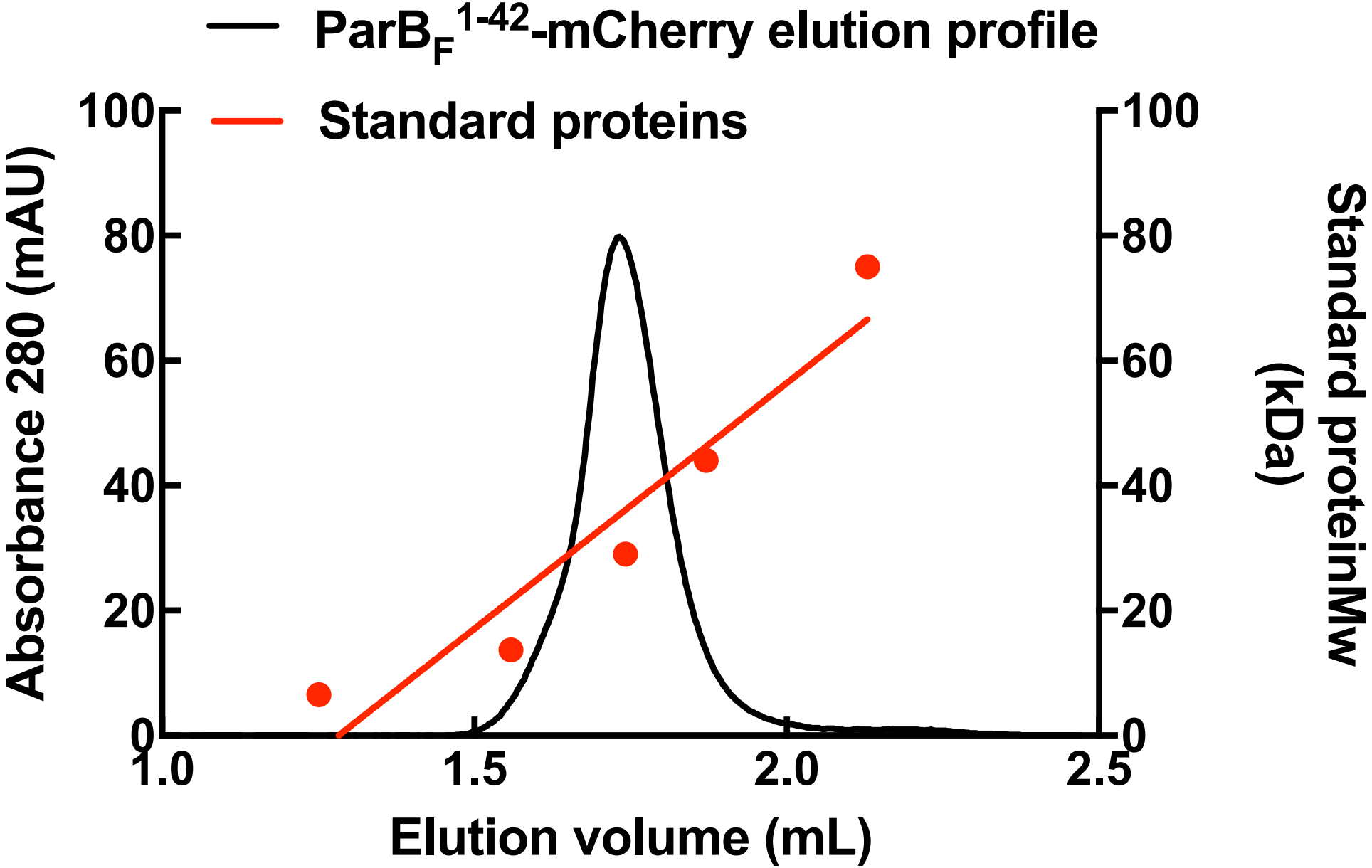
ParB$_F^{1-42}$-mCherry elution profile
Standard proteins
Absorbance 280 (mAU)
Standard proteinMw (kDa)
Elution volume (mL)
0
20
40
60
80
100
1.0
1.5
2.0
2.5

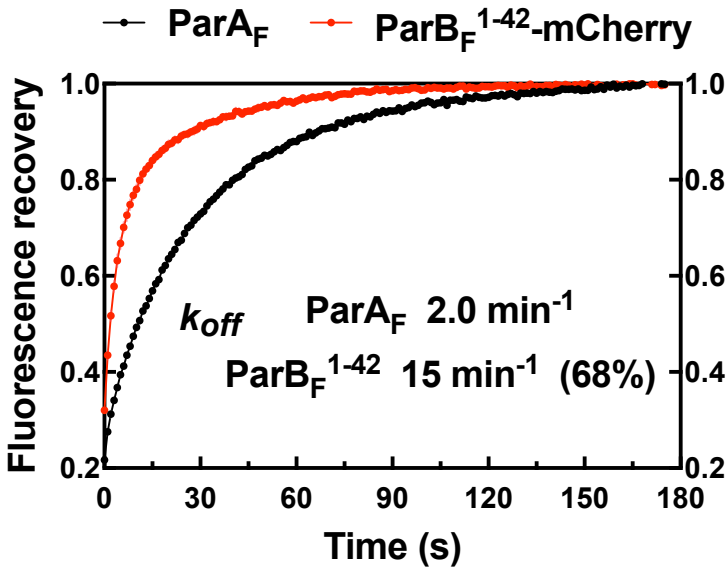
ParA$_F$
ParB$_F^{1-42}$-mCherry
Fluorescence recovery
1.0
0.8
0.6
0.4
0.2
0
30
60
90
120
150
180
Time (s)
k_{off}
ParA$_F$ 2.0 min^{-1}
ParB$_F^{1-42}$ 15 min^{-1} (68%)

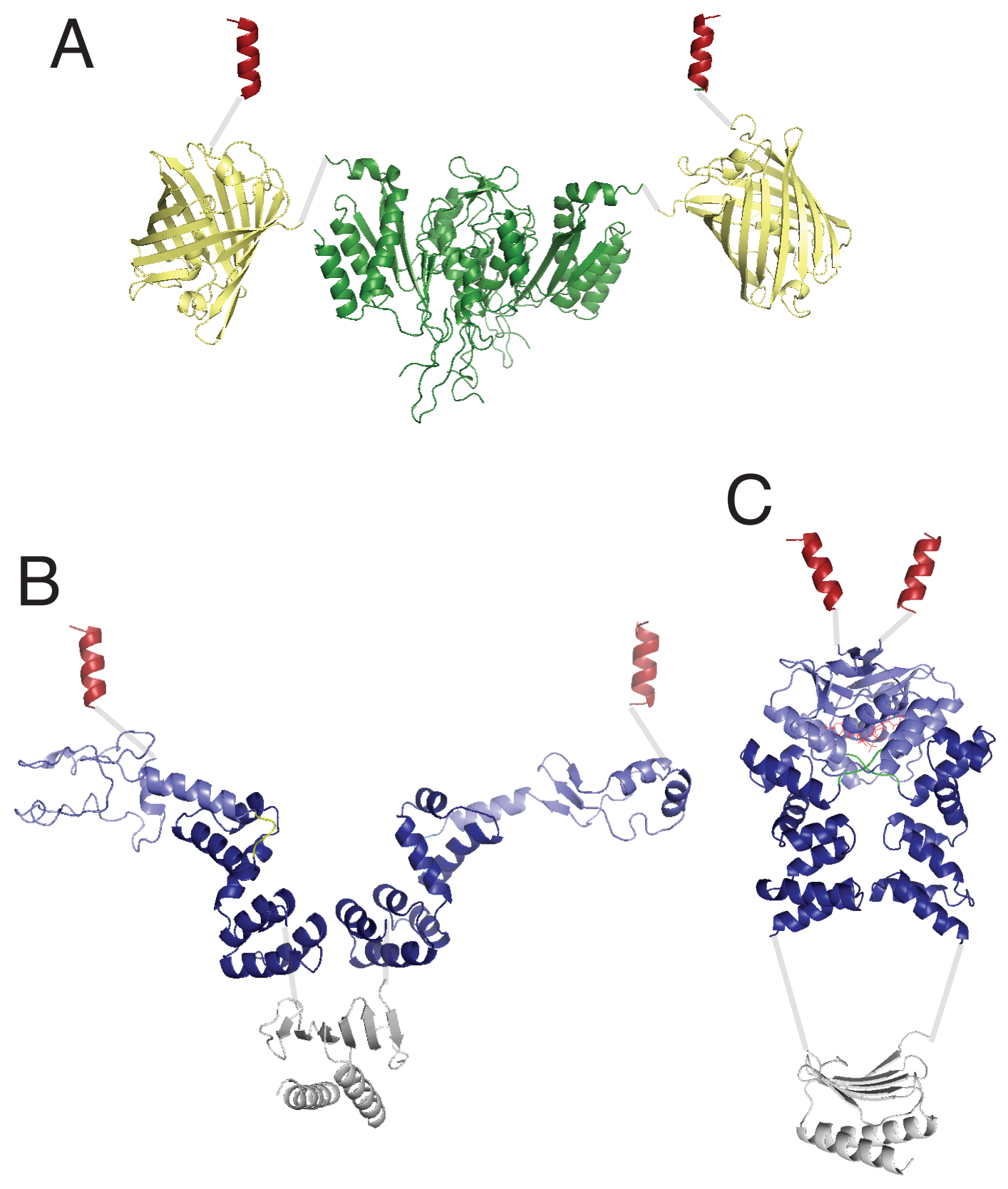
A
B
C

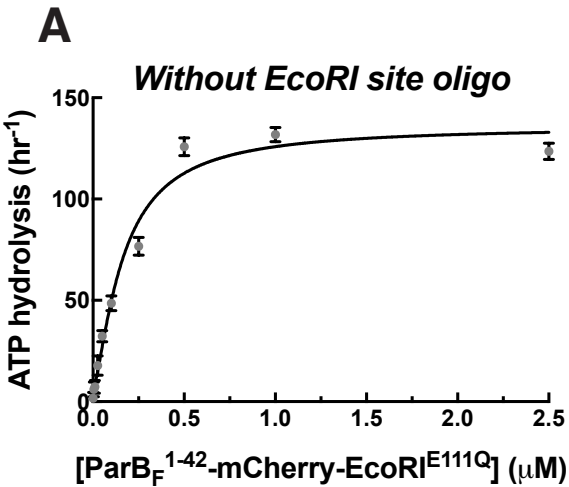
A
Without EcoRI site oligo
ATP hydrolysis (hr-1)
150
100
50
0
0.0
0.5
1.0
1.5
2.0
2.5
[ParBF1-42-mCherry-EcoRIE111Q] (μM)

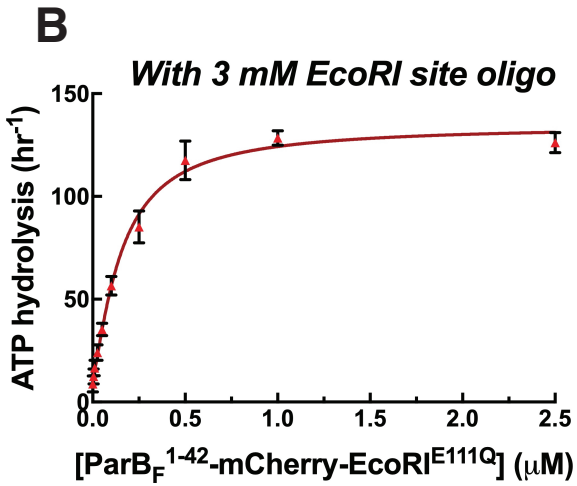
B
With 3 mM EcoRI site oligo
ATP hydrolysis (hr-1)
150
100
50
0
0.0
0.5
1.0
1.5
2.0
2.5
[ParBF1-42-mCherry-EcoRIE111Q] (μM)

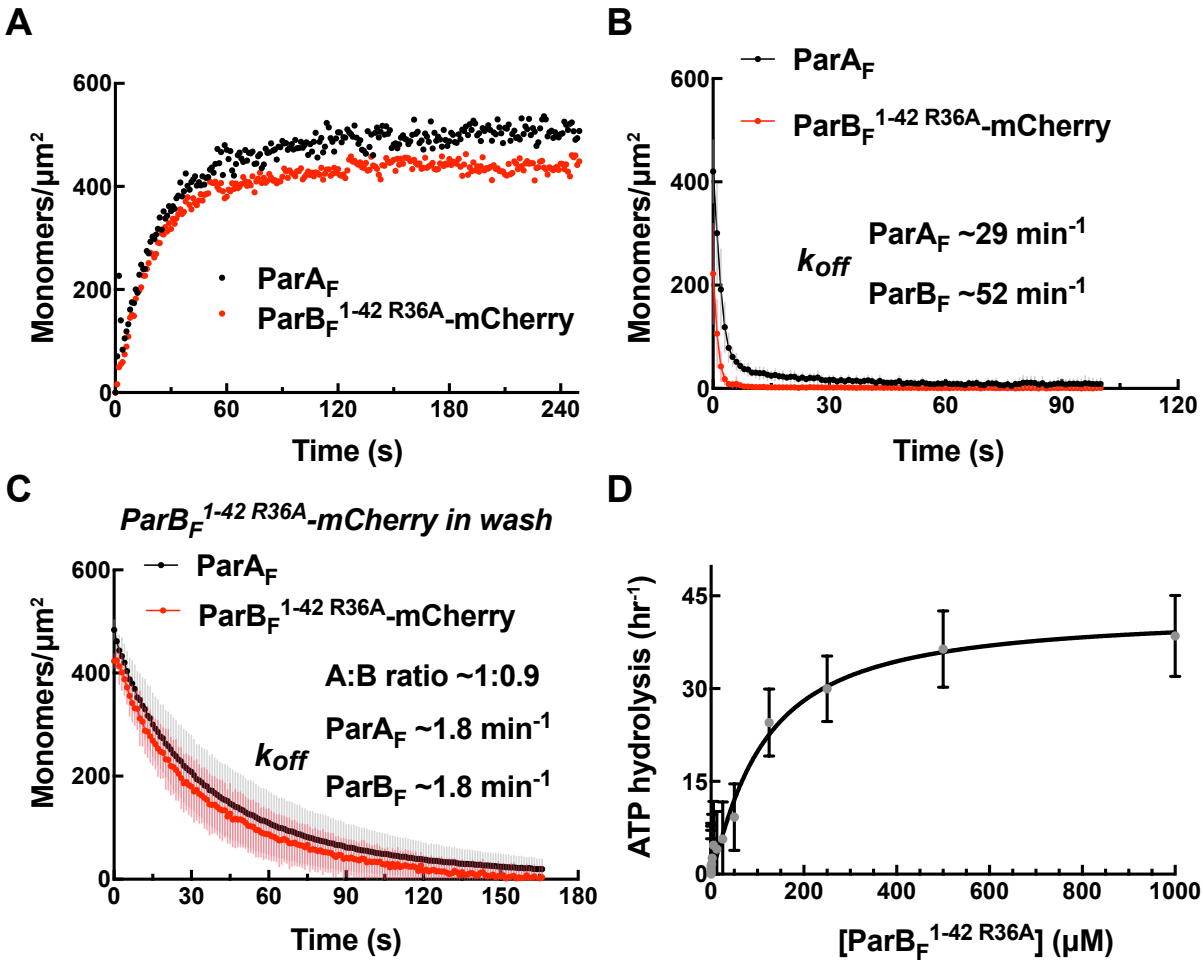
A
Monomers/μm²
600
400
200
0
0
60
120
180
240
Time (s)
ParAF
ParBF1-42 R36A-mCherry
B
ParAF
ParBF1-42 R36A-mCherry
koff
ParAF ~29 min-1
ParBF ~52 min-1
Monomers/μm²
600
400
200
0
0
30
60
90
120
Time (s)
C
ParBF1-42 R36A-mCherry in wash
ParAF
ParBF1-42 R36A-mCherry
A:B ratio ~1:0.9
koff
ParAF ~1.8 min-1
ParBF ~1.8 min-1
Monomers/μm²
600
400
200
0
0
30
60
90
120
150
180
Time (s)
D
ATP hydrolysis (hr-1)
45
30
15
0
0
200
400
600
800
1000
[ParBF1-42 R36A] (μM)

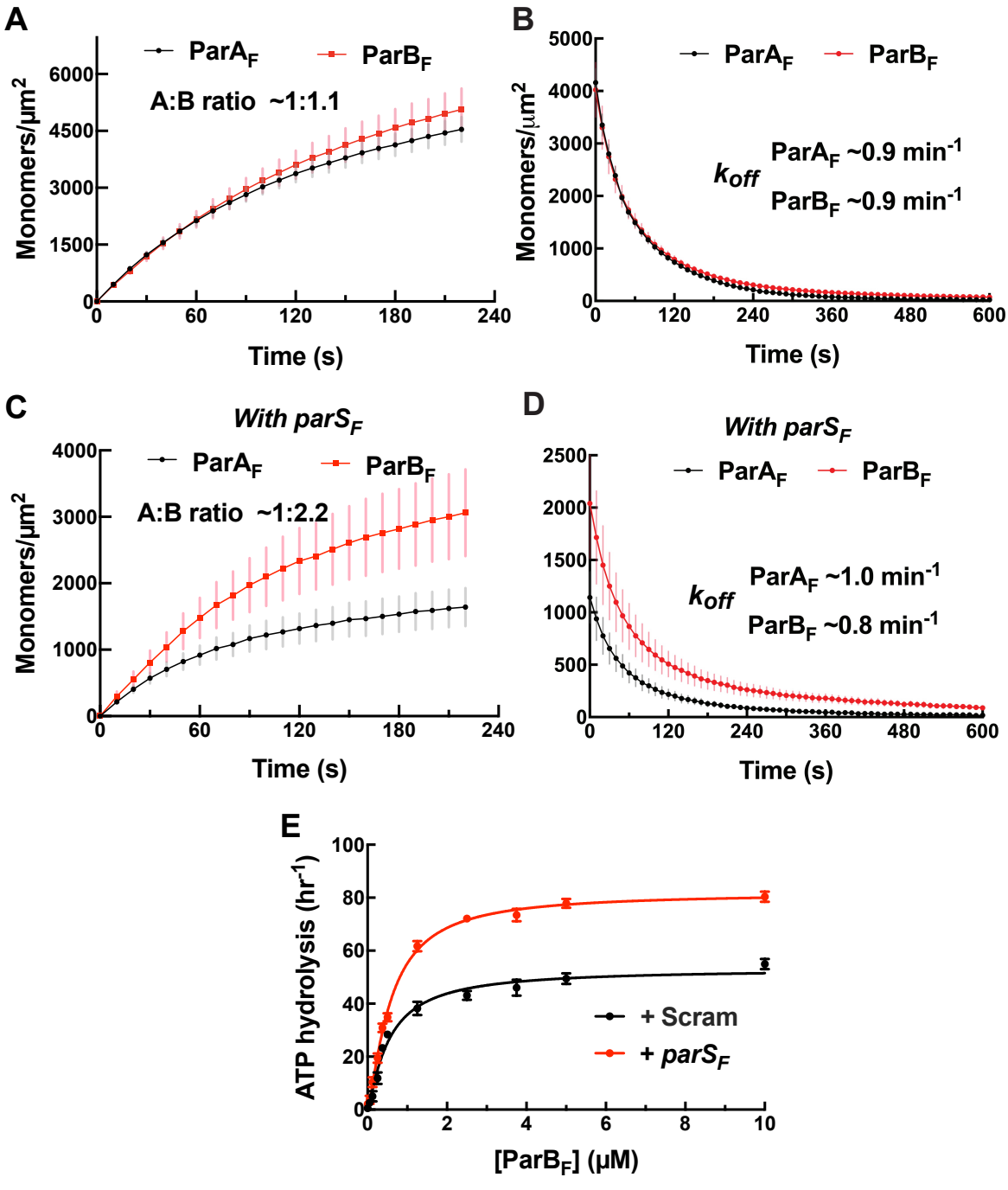
A
ParA$_F$
ParB$_F$
A:B ratio ~1:1.1
Monomers/μm^2
Time (s)
B
ParA$_F$
ParB$_F$
k_{off}
ParA$_F$ ~0.9 min^{-1}
ParB$_F$ ~0.9 min^{-1}
Monomers/μm^2
Time (s)
C
With parS$_F$
ParA$_F$
ParB$_F$
A:B ratio ~1:2.2
Monomers/μm^2
Time (s)
D
With parS$_F$
ParA$_F$
ParB$_F$
k_{off}
ParA$_F$ ~1.0 min^{-1}
ParB$_F$ ~0.8 min^{-1}
Time (s)
E
ATP hydrolysis (hr^{-1})
+ Scram
+ *parS$_F$*
[ParB$_F$] (μM)

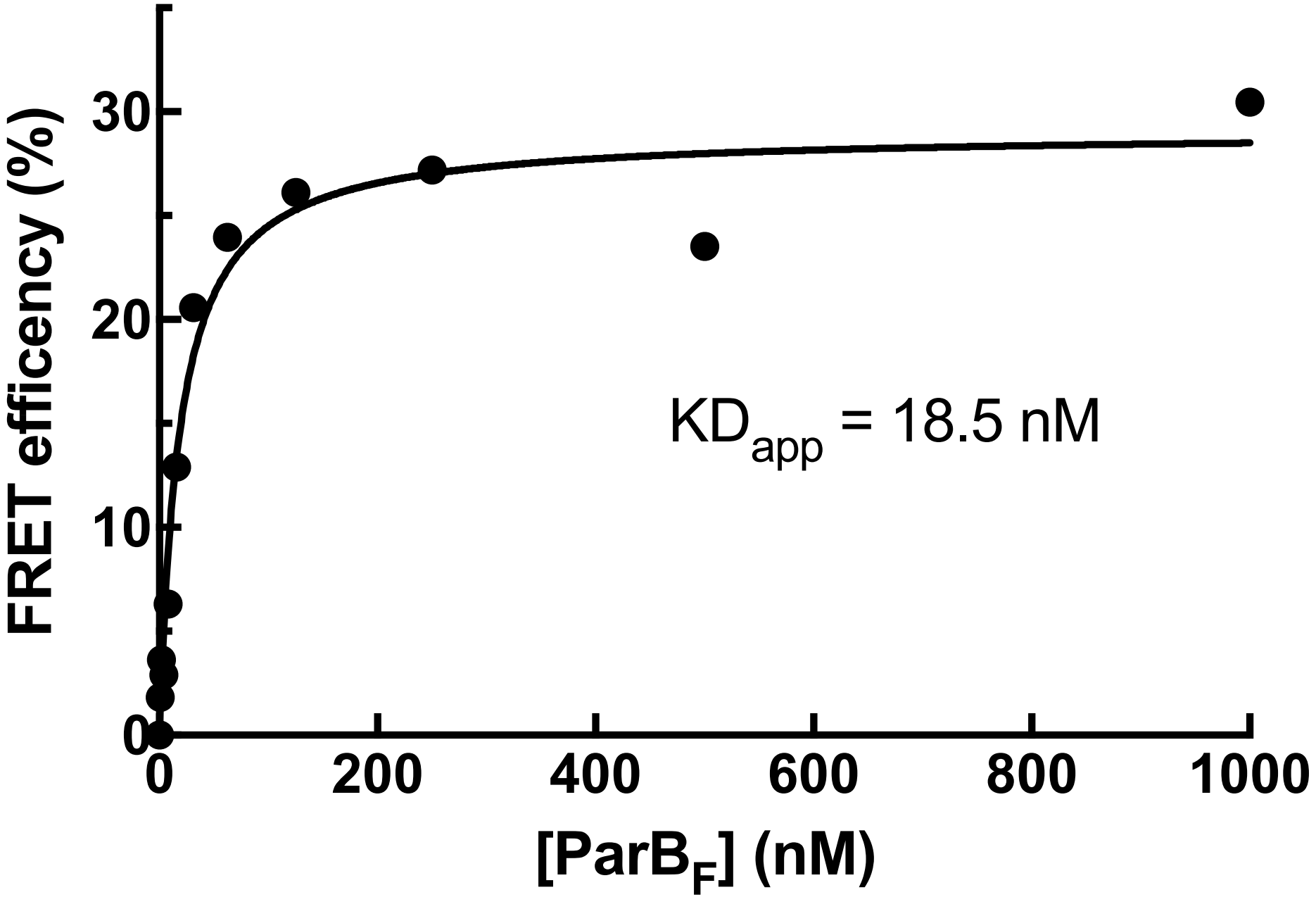
FRET efficency (%)
30
20
10
0
0
200
400
600
800
1000
[ParB$_F$] (nM)
KD$_{app}$ = 18.5 nM

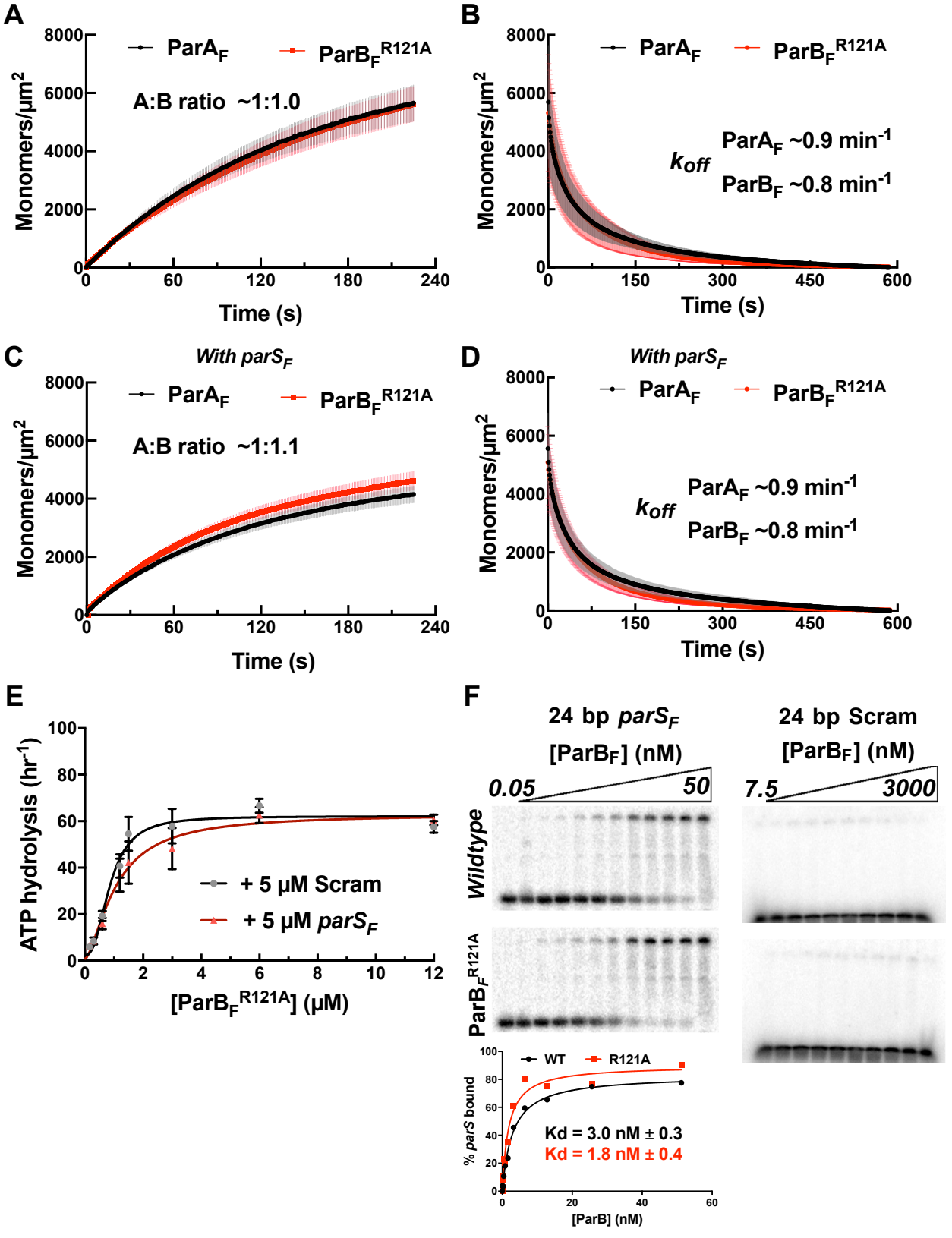
A
ParA$_F$
ParB$_F^{R121A}$
A:B ratio ~1:1.0
Monomers/µm^2
Time (s)
B
ParA$_F$
ParB$_F^{R121A}$
k_{off}
ParA$_F$ ~0.9 min^{-1}
ParB$_F$ ~0.8 min^{-1}
Monomers/µm^2
Time (s)
C
With parS$_F$
ParA$_F$
ParB$_F^{R121A}$
A:B ratio ~1:1.1
Monomers/µm^2
Time (s)
D
With parS$_F$
ParA$_F$
ParB$_F^{R121A}$
k_{off}
ParA$_F$ ~0.9 min^{-1}
ParB$_F$ ~0.8 min^{-1}
Monomers/µm^2
Time (s)
E
ATP hydrolysis (hr^{-1})
+ 5 µM Scram
+ 5 µM parS$_F$
[ParB$_F^{R121A}$] (µM)
F
24 bp parS$_F$
[ParB$_F$] (nM)
0.05
50
24 bp Scram
[ParB$_F$] (nM)
7.5
3000
Wildtype
ParB$_F^{R121A}$
WT
R121A
% parS bound
Kd = 3.0 nM ± 0.3
Kd = 1.8 nM ± 0.4
[ParB] (nM)

Figure S8

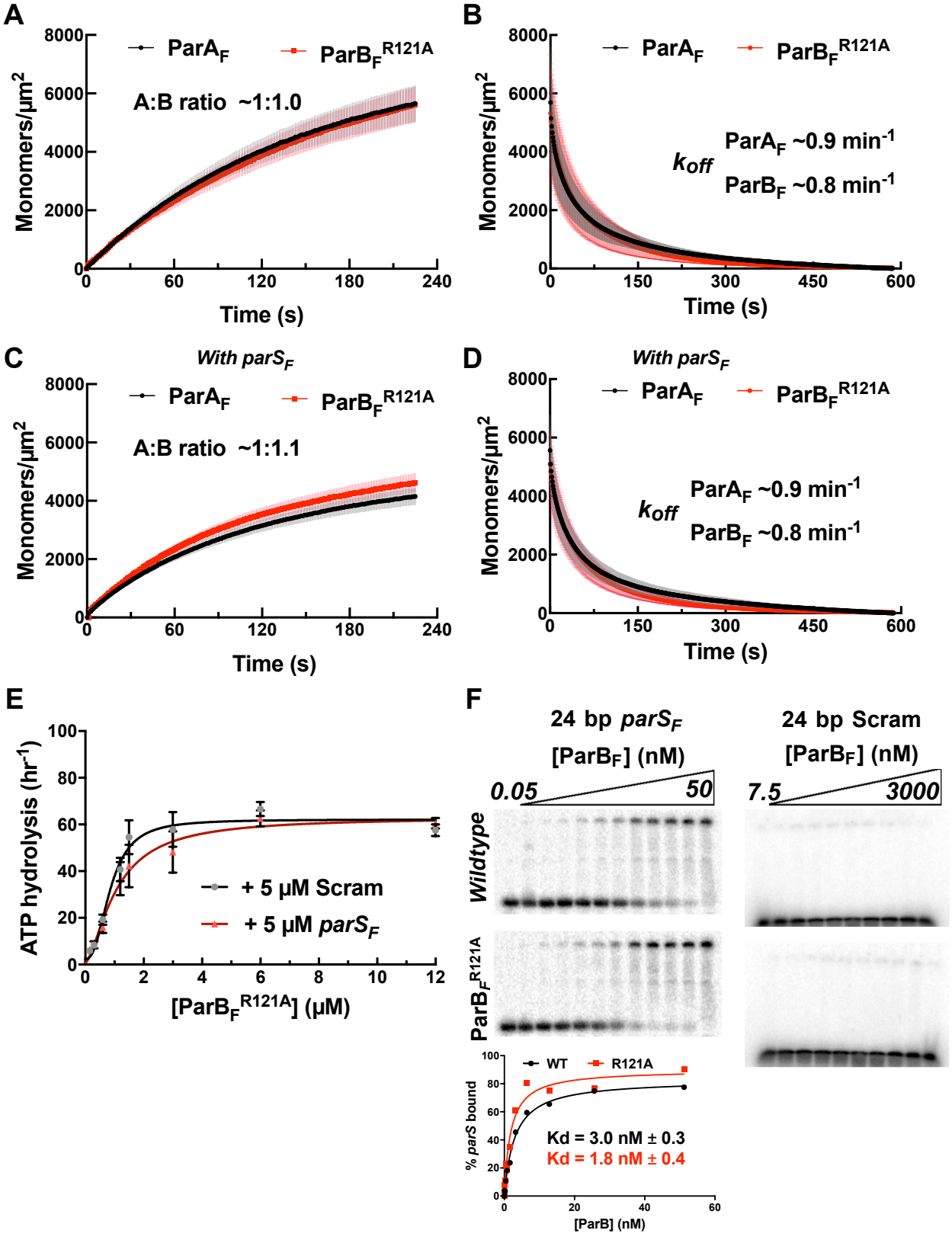
A
ParA$_F$
ParB$_F^{R121A}$
A:B ratio ~1:1.0
Monomers/µm^2
Time (s)
B
ParA$_F$
ParB$_F^{R121A}$
k_{off}
ParA$_F$ ~0.9 min^{-1}
ParB$_F$ ~0.8 min^{-1}
Monomers/µm^2
Time (s)
C
With parS$_F$
ParA$_F$
ParB$_F^{R121A}$
A:B ratio ~1:1.1
Monomers/µm^2
Time (s)
D
With parS$_F$
ParA$_F$
ParB$_F^{R121A}$
k_{off}
ParA$_F$ ~0.9 min^{-1}
ParB$_F$ ~0.8 min^{-1}
Monomers/µm^2
Time (s)
E
ATP hydrolysis (hr^{-1})
+ 5 µM Scram
+ 5 µM parS$_F$
[ParB$_F^{R121A}$] (µM)
F
24 bp parS$_F$
[ParB$_F$] (nM)
0.05
50
24 bp Scram
[ParB$_F$] (nM)
7.5
3000
Wildtype
ParB$_F^{R121A}$
WT
R121A
% parS bound
Kd = 3.0 nM ± 0.3
Kd = 1.8 nM ± 0.4
[ParB] (nM)

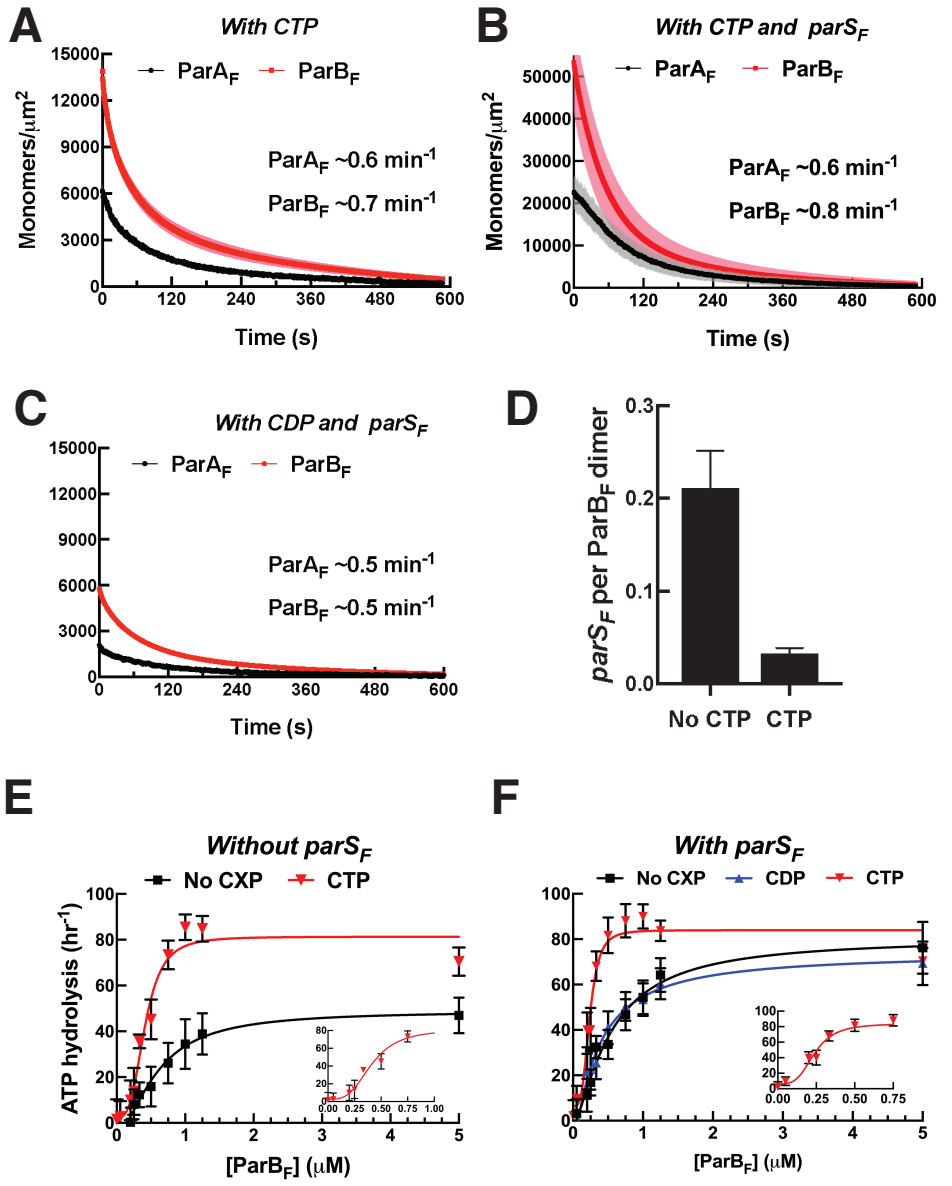
A
With CTP
ParA$_F$
ParB$_F$
ParA$_F$ ~0.6 min^{-1}
ParB$_F$ ~0.7 min^{-1}
Monomers/μm^2
Time (s)
B
With CTP and parS$_F$
ParA$_F$
ParB$_F$
ParA$_F$ ~0.6 min^{-1}
ParB$_F$ ~0.8 min^{-1}
Monomers/μm^2
Time (s)
C
With CDP and parS$_F$
ParA$_F$
ParB$_F$
ParA$_F$ ~0.5 min^{-1}
ParB$_F$ ~0.5 min^{-1}
Time (s)
D
parS$_F$ per ParB$_F$ dimer
No CTP
CTP
E
Without parS$_F$
No CXP
CTP
ATP hydrolysis (hr^{-1})
[ParB$_F$] (μM)
F
With parS$_F$
No CXP
CDP
CTP
[ParB$_F$] (μM)

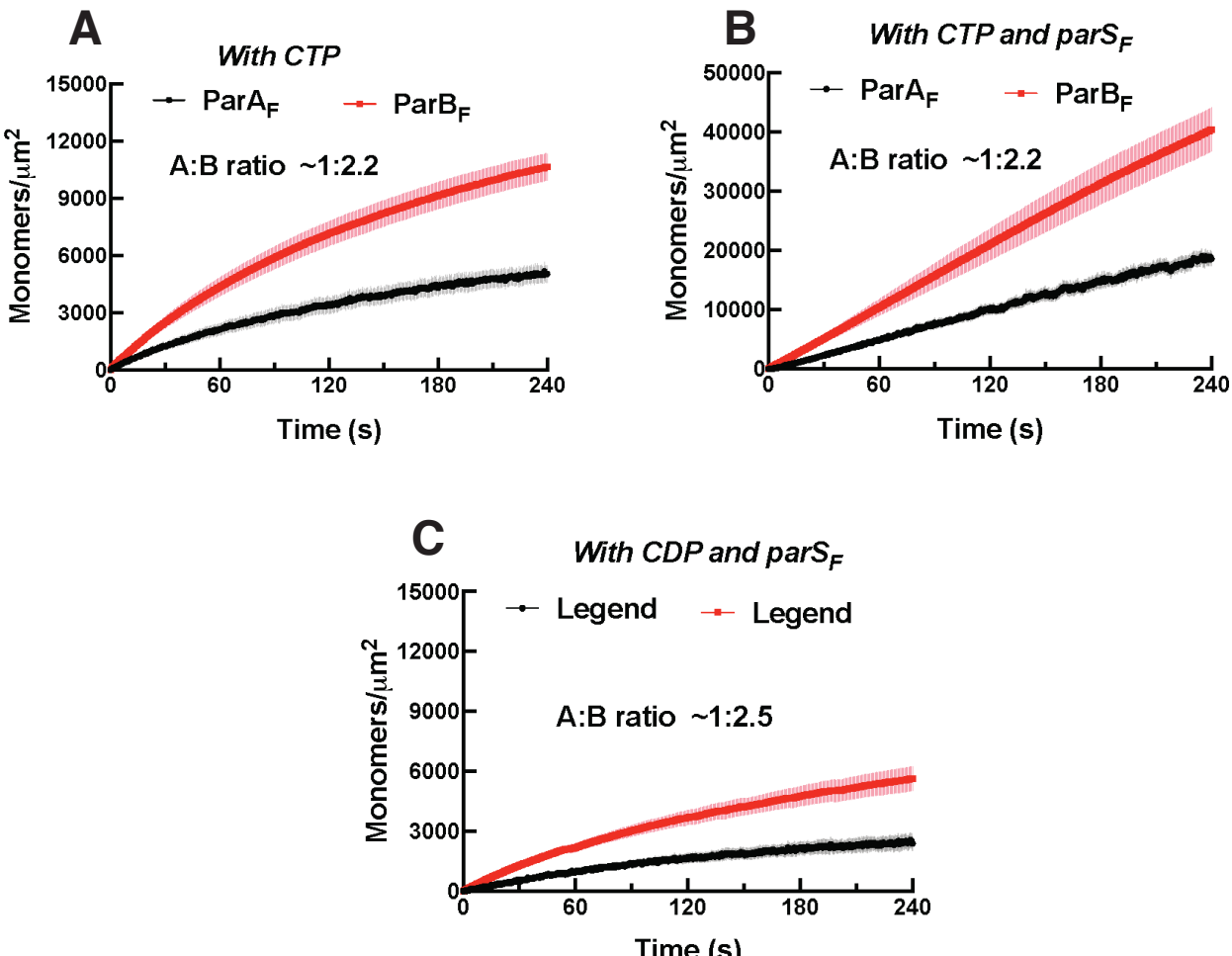
A
With CTP
ParA$_F$
ParB$_F$
A:B ratio ~1:2.2
Monomers/μm^2
15000
12000
9000
6000
3000
0
0
60
120
180
240
Time (s)
B
With CTP and parS$_F$
ParA$_F$
ParB$_F$
A:B ratio ~1:2.2
Monomers/μm^2
50000
40000
30000
20000
10000
0
0
60
120
180
240
Time (s)
C
With CDP and parS$_F$
Legend
Legend
A:B ratio ~1:2.5
Monomers/μm^2
15000
12000
9000
6000
3000
0
0
60
120
180
240
Time (s)

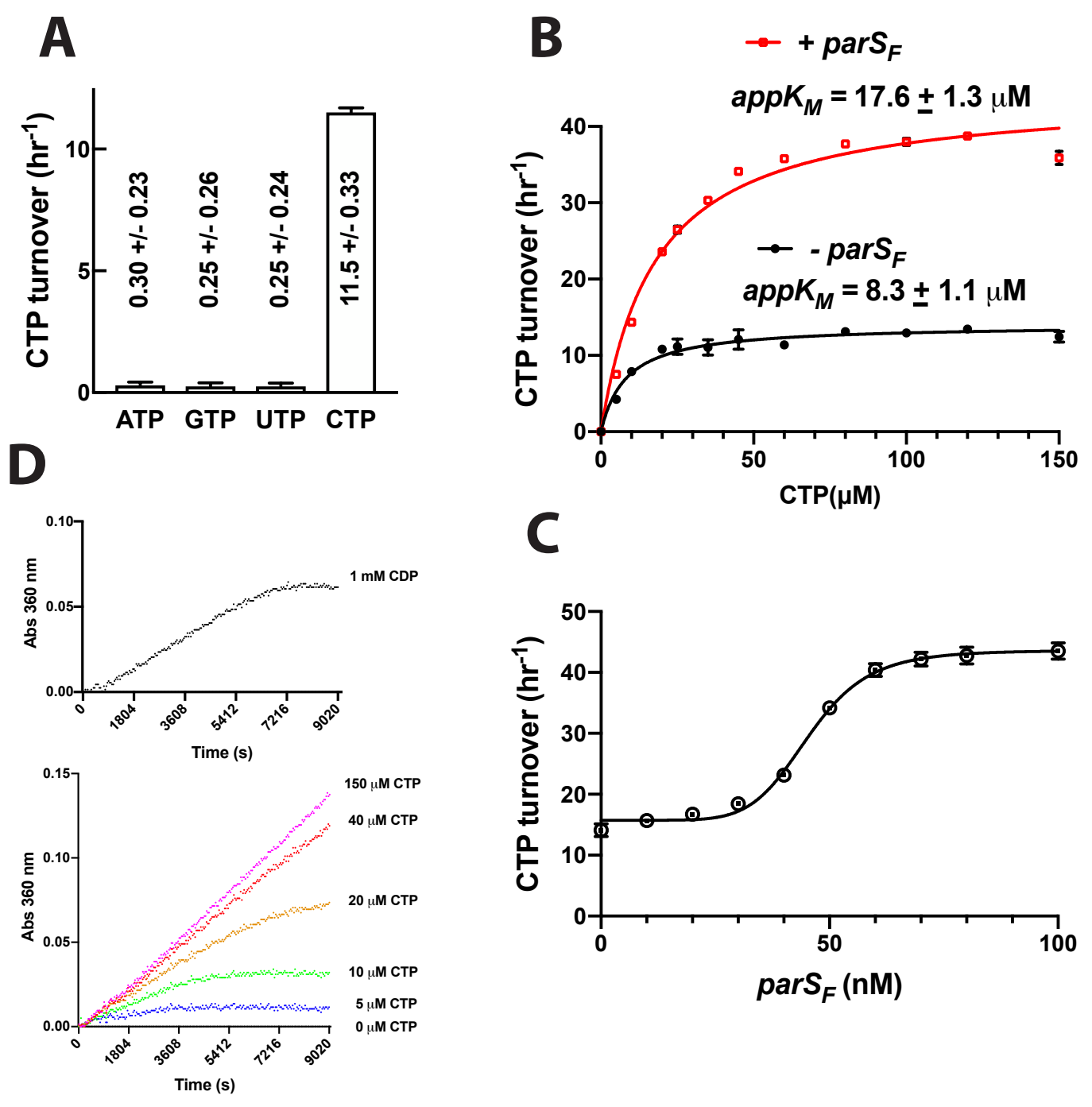
A
CTP turnover (hr-1)
0.30 +/- 0.23
0.25 +/- 0.26
0.25 +/- 0.24
11.5 +/- 0.33
ATP
GTP
UTP
CTP
B
+ parSF
appKM = 17.6 ± 1.3 μM
- parSF
appKM = 8.3 ± 1.1 μM
CTP turnover (hr-1)
CTP(μM)
C
CTP turnover (hr-1)
parSF (nM)
D
Abs 360 nm
1 mM CDP
Time (s)
150 μM CTP
40 μM CTP
20 μM CTP
10 μM CTP
5 μM CTP
0 μM CTP

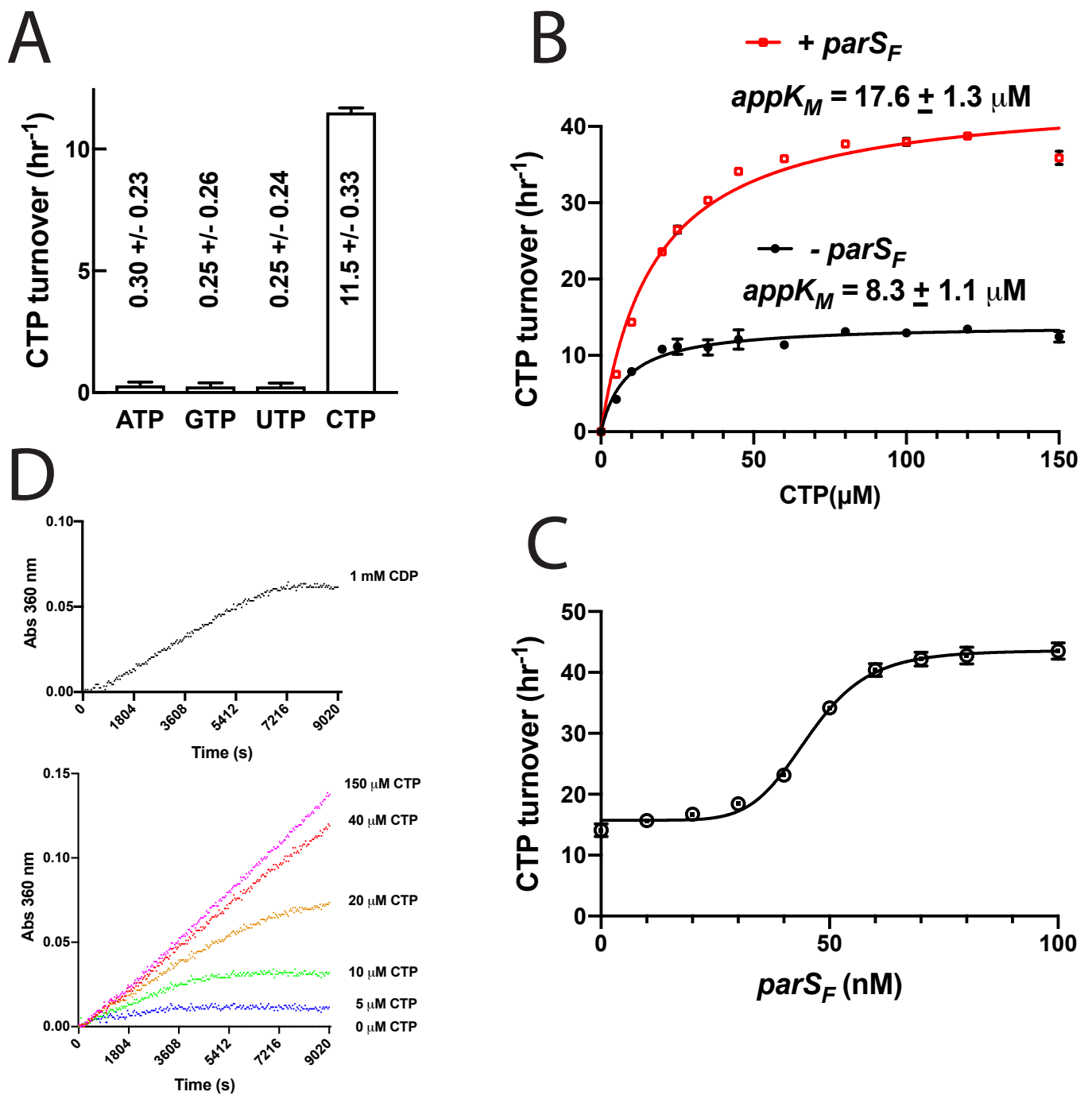
A
CTP turnover (hr-1)
0.30 +/- 0.23
0.25 +/- 0.26
0.25 +/- 0.24
11.5 +/- 0.33
ATP
GTP
UTP
CTP
B
+ parSF
appKM = 17.6 ± 1.3 μM
- parSF
appKM = 8.3 ± 1.1 μM
CTP turnover (hr-1)
CTP(μM)
C
CTP turnover (hr-1)
parSF (nM)
D
Abs 360 nm
1 mM CDP
Time (s)
150 μM CTP
40 μM CTP
20 μM CTP
10 μM CTP
5 μM CTP
0 μM CTP

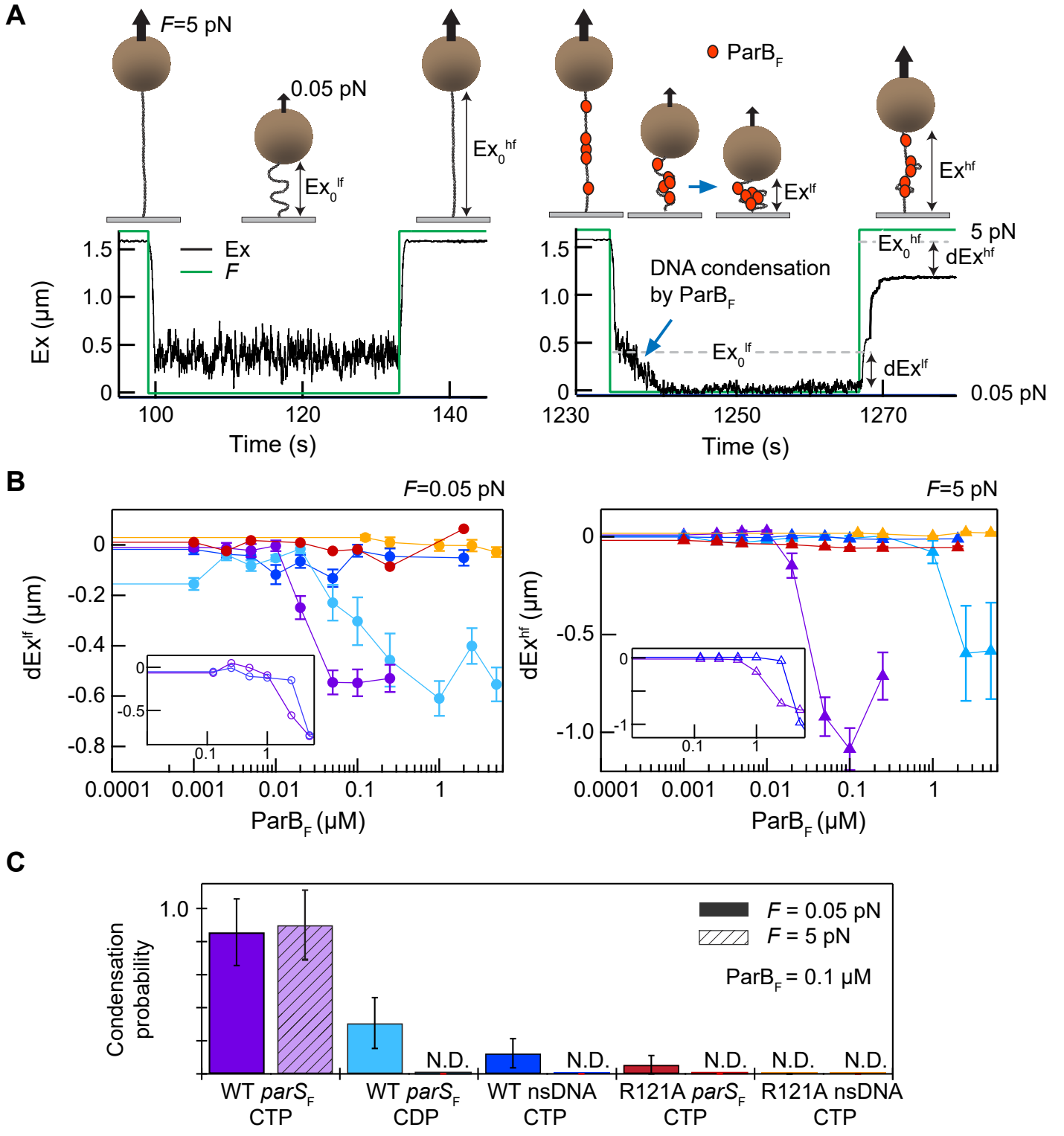
A
F=5 pN
0.05 pN
Ex0hf
Ex0lf
ParBF
Exlf
Exhf
Ex
F
Ex (µm)
Time (s)
DNA condensation
by ParBF
5 pN
dExhf
dExlf
0.05 pN
B
F=0.05 pN
F=5 pN
dExlf (µm)
dExhf (µm)
ParBF (µM)
C
Condensation probability
F = 0.05 pN
F = 5 pN
ParBF = 0.1 µM
N.D.
WT parSF CTP
WT parSF CDP
WT nsDNA CTP
R121A parSF CTP
R121A nsDNA CTP

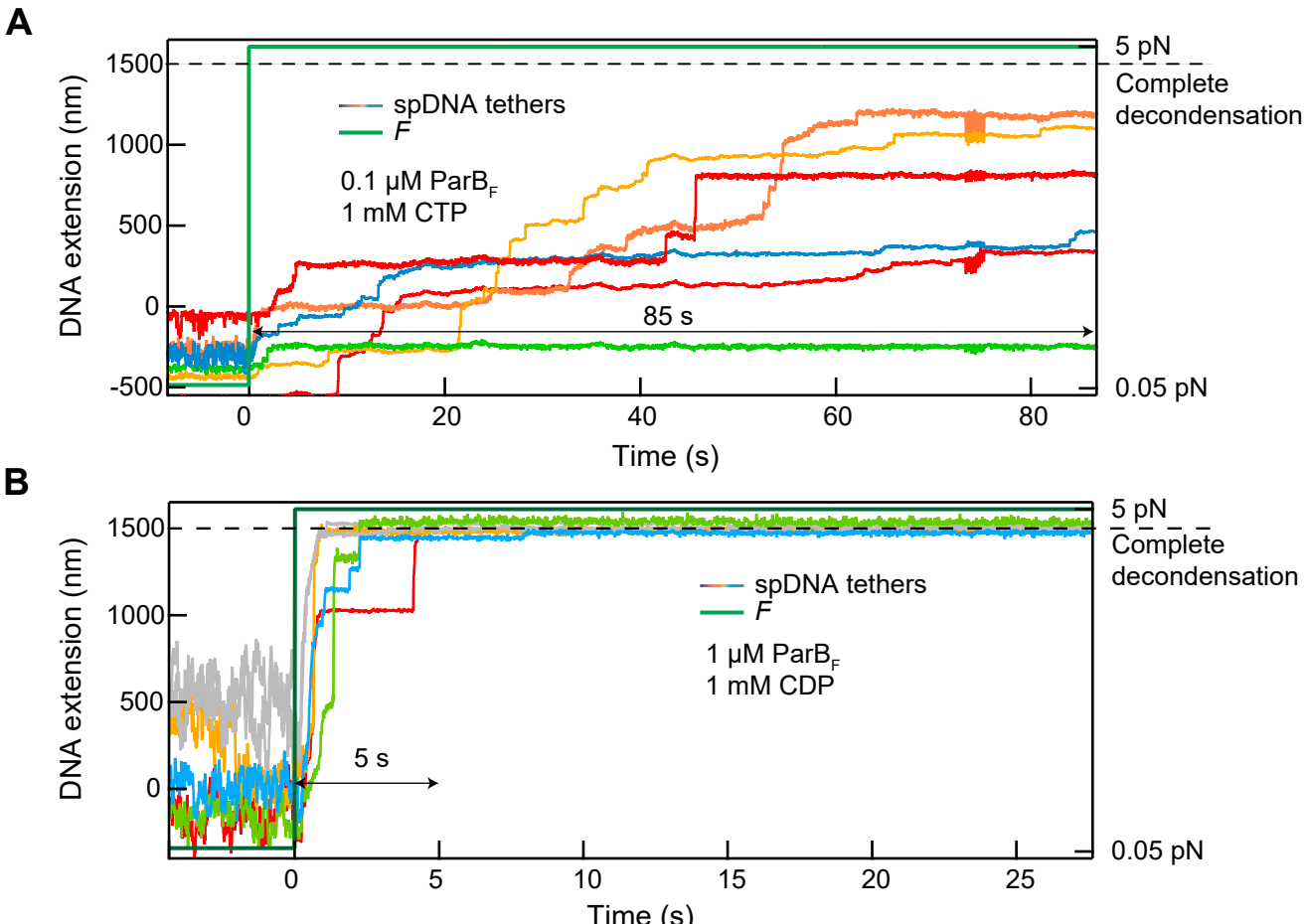
A
DNA extension (nm)
1500
1000
500
0
-500
spDNA tethers
F
0.1 μM ParB$_F$
1 mM CTP
85 s
5 pN
Complete decondensation
0.05 pN
0
20
40
60
80
Time (s)
B
DNA extension (nm)
1500
1000
500
0
spDNA tethers
F
1 μM ParB$_F$
1 mM CDP
5 s
5 pN
Complete decondensation
0.05 pN
0
5
10
15
20
25
Time (s)

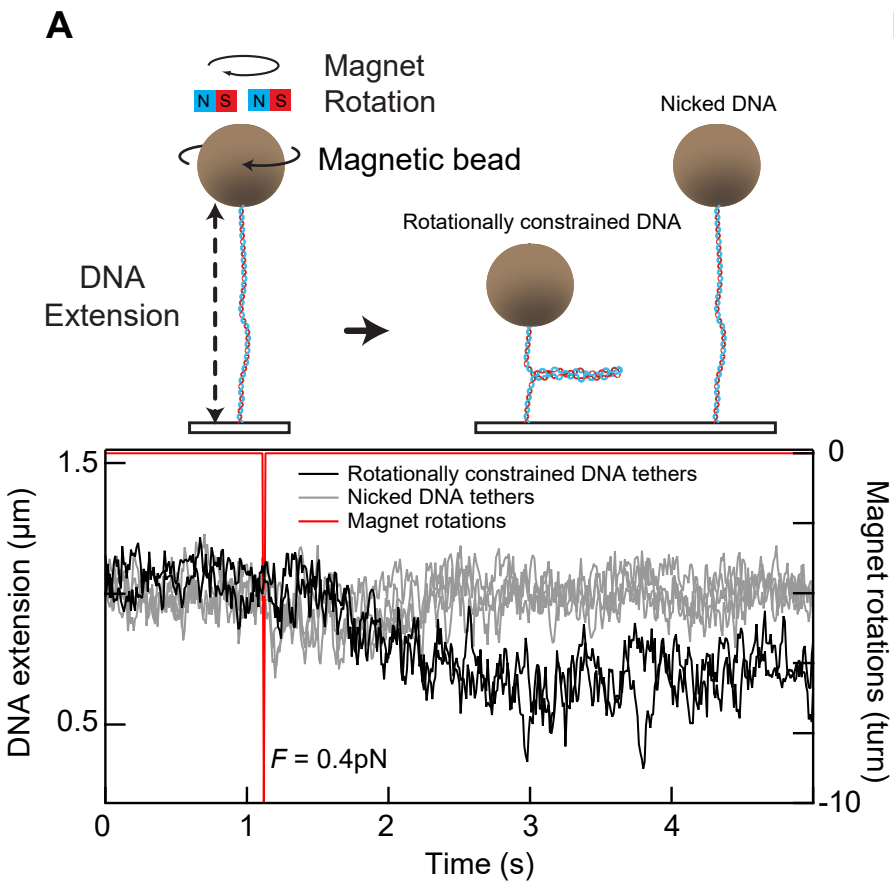
A
Magnet
Rotation
N S N S
Nicked DNA
Magnetic bead
Rotationally constrained DNA
DNA
Extension
Rotationally constrained DNA tethers
Nicked DNA tethers
Magnet rotations
F = 0.4pN
DNA extension (μm)
Magnet rotations (turn)
Time (s)
1.5
0.5
0
-10
0
1
2
3
4

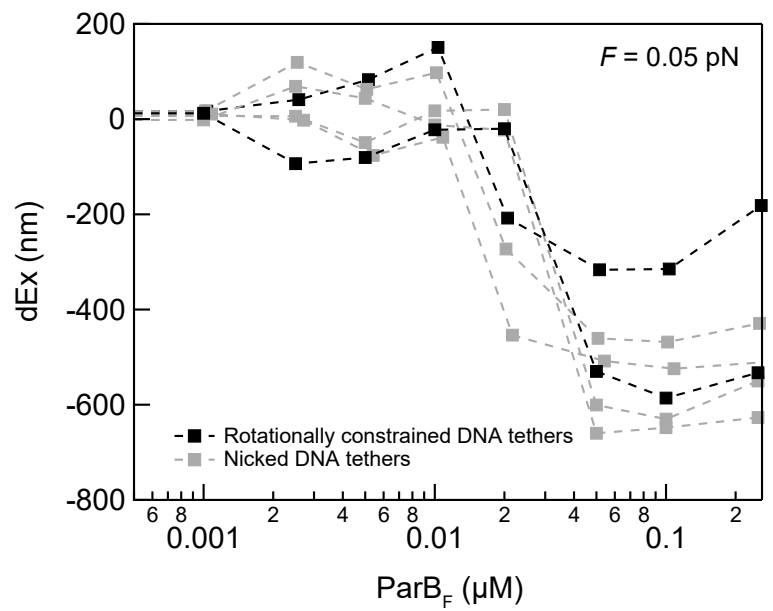
B
F = 0.05 pN
dEx (nm)
200
0
-200
-400
-600
-800
Rotationally constrained DNA tethers
Nicked DNA tethers
0.001
0.01
0.1
ParB$_F$ (μM)

No nsDNA tether condensation by adding $ParB_F$ and $parS_F$ oligo

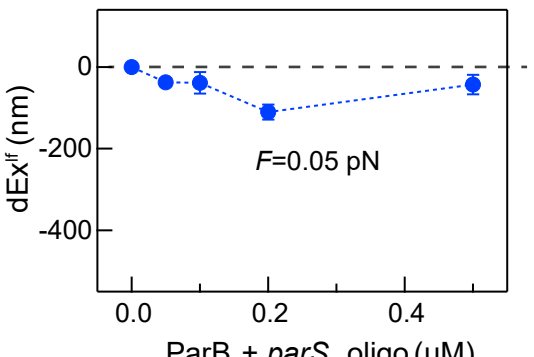

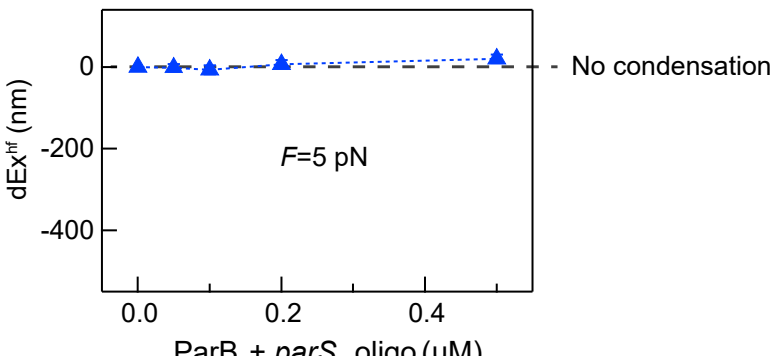

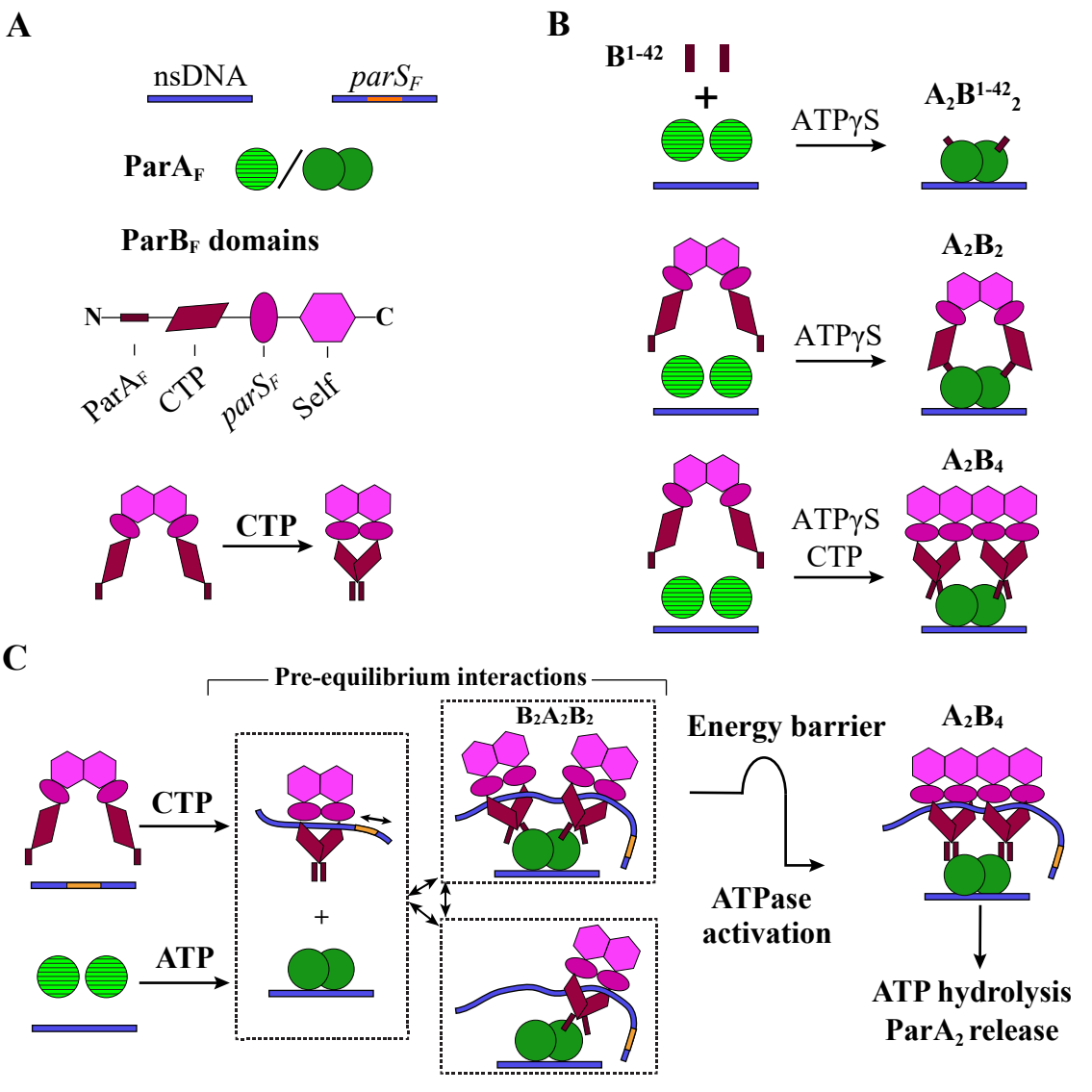
A
nsDNA
parS_F
ParA_F
ParB_F domains
N
C
ParA_F
CTP
parS_F
Self
CTP
B
B1-42
+
ATPγS
A2B1-42 2
A2B2
ATPγS
A2B4
ATPγS
CTP
C
Pre-equilibrium interactions
CTP
ATP
+
B2A2B2
Energy barrier
ATPase activation
A2B4
ATP hydrolysis
ParA2 release